The Astrophysical Journal, 794:95 (21pp), 2014 October 10 doi:10.1088/0004-637X/794/1/95

A NEW METHOD TO OBTAIN THE BROAD LINE REGION SIZE OF HIGH REDSHIFT QUASARS*

C. Alenka Negrete[1], Deborah Dultzin[2], Paola Marziani[3], and Jack W. Sulentic[4]
[1] Instituto Nacional de Astrofísica, Óptica y Electrónica, Mexico; cnegrete@inaoep.mx
[2] Instituto de Astronomía, Universidad Nacional Autónoma de México, Mexico; deborah@astro.unam.mx
[3] INAF, Astronomical Observatory of Padova, Italy; paola.marziani@oapd.inaf.it
[4] Instituto de Astrofísica de Andalucía, Spain; sulentic@iaa.es
Received 2014 January 23; accepted 2014 August 20; published 2014 September 25

ABSTRACT

We present high signal-to-noise ratio UV spectra for eight quasars at $z \sim 3$ obtained with Very Large Telescope/FORS. The spectra enable us to analyze in detail the strong and weak emission features in the rest frame range 1300–2000 Å of each source (C III] λ1909, Si III] λ1892, Al III λ1860, Si II λ1814, C IV λ1549 and blended Si IV λ1397+O IV] λ1402). The flux ratios Al III λ1860/Si III] λ1892, C IV λ1549/Al III λ1860, Si IV λ1397+O IV] λ1402/Si III] λ1892 and Si IV λ1397+O IV] λ1402/C IV λ1549 strongly constrain ionizing photon flux and metallicity through the use of diagnostic maps built from CLOUDY simulations. The radius of the broad line region is then derived from the ionizing photon flux applying the definition of the ionization parameter. The $r_{\rm BLR}$ estimate and the width of a virial component isolated in prominent UV lines yields an estimate of black hole mass. We compare our results with previous estimates obtained from the $r_{\rm BLR}$–luminosity correlation customarily employed to estimate the black hole masses of high redshift quasars.

Key words: galaxies: active – galaxies: high-redshift – quasars: emission lines – quasars: general

Online-only material: color figures

1. INTRODUCTION

Measuring relevant physical parameters from the observed broad-line spectra of quasars is still an open challenge. Identification and intensity measurements of the strongest emission lines have made possible a rough inference about typical conditions in the emitting gas from the earliest days of quasar spectroscopy. The first intermediate redshift quasars discovered in the 1960s showed a fairly high ionization spectrum with prominent lines of C IV λ1549 and He II λ1640 in addition to the strong Balmer lines seen in the lower redshift sources. Photoionization by a central continuum source was considered the principal heating mechanism of the emitting gas. Significant C III] λ1909 emission suggested electron densities (n_e) in the range 10^9–10^{10} cm^{-3}. The observed intensity ratio C III] λ1909/C IV λ1549 indicated ionization parameter (U; defined by Equation (1) later in this paper) values of the order of 10^{-1}. This photoionization scenario was successful in explaining at least some quasar optical and UV spectra (see the review by Davidson & Netzer 1979 for a synopsis).

More recent work recognized the existence of several problems with the original scenario. Low ionization lines (LILs), and especially Fe II are too strong to be explained by a photoionized region of moderate density and column density (see, for example, Dumont & Mathez 1981; Joly 1987; Collin-Souffrin et al. 1988; Collin-Souffrin & Dumont 1990). These authors stressed that the LILs required a denser, low-temperature environment. Even more recently, Baldwin et al. (1996), Laor et al. (1997a), and Baldwin et al. (2004) point toward high density at least for the LIL emitting zone. This low ionization broad line region (LIL BLR) has very similar properties to the O I and Ca II emitting region identified by Matsuoka et al. (2008). The region where these LILs are produced cannot emit much C III] λ1909 if the electron density exceeds 10^{11} cm^{-3}. BLR conditions are certainly complex and the assumption of a single emitting region cannot explain both LILs and high ionization lines (HILs) in all quasars (Marziani et al. 2010; Wang et al. 2011 and references therein).

In Negrete et al. (2012, hereafter Paper I), we report an analysis based on several diagnostic ratios used to constrain density, ionization parameter, and metallicity in the BLR of two sources that are representative of extreme Population A (Pop A; narrow line Seyfert 1—NLSy1) sources. These sources showed weak C III] λ1909 emission (relative to Si III] λ1892), which simplified our interpretation of the emission line spectra. Diagnostic ratios indicate a very dense ($n_e \sim 10^{12}$ cm^{-3}), low ionization ($U \sim 10^{-2.7}$) region that, in a photoionization scenario, is expected to also emit Fe II and Ca II lines (e.g., Brühweiler & Verner 2008; Matsuoka et al. 2008). In Negrete et al. (2013, hereafter Paper II), we show that C III] λ1909 is not associated with the high density region. However C III] λ1909 is strong in most sources, dominating the emission of the 1900 Å blend. The presence of strong C III] λ1909 indicates that the BLR can no longer be characterized by a narrow range of density and ionization parameter: a gradient of ionization, density, or both may be present. Since the BLR is not spatially resolved, the meaning of the emission line ratios becomes much more ambiguous, and we cannot obtain meaningful single-value measures of $n_{\rm H}$ and ionization. Nonetheless, the ionizing photon flux (i.e., the product $n_{\rm H}U$) can be retrieved with an accuracy comparable to estimates obtained from reverberation mapping (RM), and then used to estimate $r_{\rm BLR}$ (Paper II).

In this paper we apply the method discussed in Paper II to a pilot sample of high redshift ($z \sim 3$) sources. The technique we present should allow one to easily compute $r_{\rm BLR}$ for large samples of high z sources. Moderate resolution and high signal-to-noise ratio (S/N) dedicated observations allowed us to detect and measure faint and blended lines in order to analyze all physical information that can be retrieved from

* Based on observations made with ESO Telescopes at Paranal Observatory under program ID 078.B-0109(A).

Table 1
Basic Properties of Sources and Log of Observations

Object Name (1)	m_B (2)	z (3)	Δ_z (4)	Line (5)	M_B (6)	Flux 6cm (mJy) (7)	Date (8)	DIT (9)	N_{exp} (10)	Airmass (11)	S/N (12)
J00103−0037	18.39	3.1546	0.0052	1	−25.68	0.402	2006 Nov 8	1139	3	1.13	60
J00521−1108	18.70	3.2364	0.0018	2	−25.39	0.432	2007 Jan 1	1199	3	1.22	41
J01225+1339	18.24	3.0511	0.0011	1	−25.80	[a]	2006 Nov 8	1259	2	1.34	92
J02287+0002	18.20	2.7282	0.0097	1	−25.72	0.351	2006 Dec 16	1259	2	1.11	67
J02390−0038	18.68	3.0675	0.0083	1	−25.36	0.429	2006 Nov 7	1199	3	1.47	57
J03036−0023	17.65	3.2319	0.0016	1	−26.44	0.339	2006 Dec 16	1259	2	1.13	88
J20497−0554	18.29	3.1979	0.0068	1	−25.79	[a]	2006 Nov 4	1259	2	1.61	54
J23509−0052	18.67	3.0305	0.0041	1	−25.36	0.411	2006 Nov 7	1199	3	1.12	62

Note. [a] Not in FIRST.

rest frame UV spectra of high-z quasars. The pilot sample helps us explore challenges that exist for studying high-z sources using only rest frame UV spectra. The estimation of redshift cannot rely on measures of low-ionization narrow lines that are the most credible diagnostics at low z. (Eracleous & Halpern 2003; Hu et al. 2008). Narrow lines are weak and often undetectable in very high luminosity sources (Marziani et al. 2009), a phenomenon sometimes called the [O III] λλ4959, 5007 Baldwin effect (Zhang et al. 2011). On the other hand, the criteria for population and spectral type identification were set from properties of the Hβ spectral range (Sulentic et al. 2000), which is customarily not available for high z quasars.

We present the spectra of eight pilot sources obtained with the Very Large Telescope (VLT)/FORS1 in Section 2; Section 3 summarizes data reduction, including details of redshift estimation (Section 3.2). Before discussing the analysis of the data, we present a synopsis of quasar systematics along the so-called eigenvector 1 (E1), with special attention on the interpretation of the line profiles. In Section 4 we apply the interpretation of the line profiles derived from low-z sources to fit the line profiles in this high-z sample. In Section 5 we discuss the population assignment and the properties of each source, while Section 6 explores BLR physical conditions, with special reference to metallicity issues (Section 6.3). Section 7 presents results from the application of the photoionization method to our pilot sample. Section 8 presents derivations of the BLR radius (r_{BLR}; its distance from the ionizing source), and black hole mass (M_{BH}). Section 9 compares our results with previous work and Section 10 considers the prospects for the application of our technique for single epoch M_{BH} estimates in high redshift samples. All the computations were made considering $H_0 = 70$ km s^{-1} Mpc^{-1} and relative energy densities $\Omega_\Lambda = 0.7$ and $\Omega_M = 0.3$.

2. OBSERVATIONS

Data were obtained between 2006 November and 2007 January using the VLT2/FORS1 telescope operated in service mode. FORS1 is the visual and near UV focal reducer and low dispersion spectrograph of the VLT operated by European Southern Observatory (ESO; Appenzeller et al. 1998). A pilot sample of eight quasars at $z \sim 3$ was observed with long exposure times to ensure high S/N in the continuum, in all cases above ≈40, and otherwise in the range 50–100. Table 1 provides a log of observations that are organized as follows: Column 1: object name; Column 2: apparent B magnitude; Column 3: redshift; Column 4: redshift uncertainty; Column 5: line used for redshift estimation: (1) O I λ1304, (2) C III] λ1909; Column 6: absolute B magnitude; Column 7: flux at 6 cm taken from FIRST (Becker et al. 1995); Column 8: date (refers to time at start of exposure); Column 9: detector integration time (DIT); Column 10: number of exposures with integration time equal to DIT; Column 11: average of the airmass; Column 12: S/N in the continuum around 1700 Å.

The observation of one of our eight quasars, J00521−1108, yielded the lowest S/N spectrum, which we retain because the observed features in the blend at ∼1900 Å are clear enough to fit the individual lines. Two sources, J01225+1339 and J02287+0002, are high-ionization, broad absorption line (BAL) quasars, with deep absorption troughs that deeply affect the C IV λ1549 emission profile.

3. DATA REDUCTION

Data were reduced using standard IRAF tasks. All spectra were wavelength and flux calibrated in the observed frame and then corrected for Galactic extinction. Flux correction was applied using meteorological data provided by ESO. The observed flux was multiplied by the inverse of the light lost computed from the ratio seeing over slit width in arcsec. Correction to rest frame requires estimating the redshift z which is not a trivial task, as outlined below. Rest frame correction also involved scaling the specific flux in flux per unit wavelength interval by a factor $(1+z)^3$. Measurements were carried out on the rest frame spectra. The following section describes two important aspects of the data reduction.

3.1. A and B Atmospheric Bands Correction

The A or B atmospheric band falls on top of the 1900 Å blend in many of the spectra. This is an important region for this study, especially because it involves Si III] λ1892, Al III λ1860, and Si II λ1814. In order to remove these absorption features we created an A+ B band template from standard star spectra used as specific flux calibrators. We scaled this template to find a best fit. Figure 1 shows the A and B absorption correction where we overtrace the uncorrected spectrum to illustrate which lines are affected. In cases where the A or B bands overlap a weak line like Si II λ1814 the effect is considerable and measures of Si II λ1814 should not be considered at all or with extreme care. This happens for sources J00103−0037, J03036−0023, and J20497−0554. In cases where one of the bands overlaps a stronger line like Si III] λ1892 or Al III λ1860, the correction was good enough to permit accurate measures.

3.2. Redshift Estimate

Normally one uses strong narrow emission lines, preferentially from low ionization ionic species, to set the rest frame in

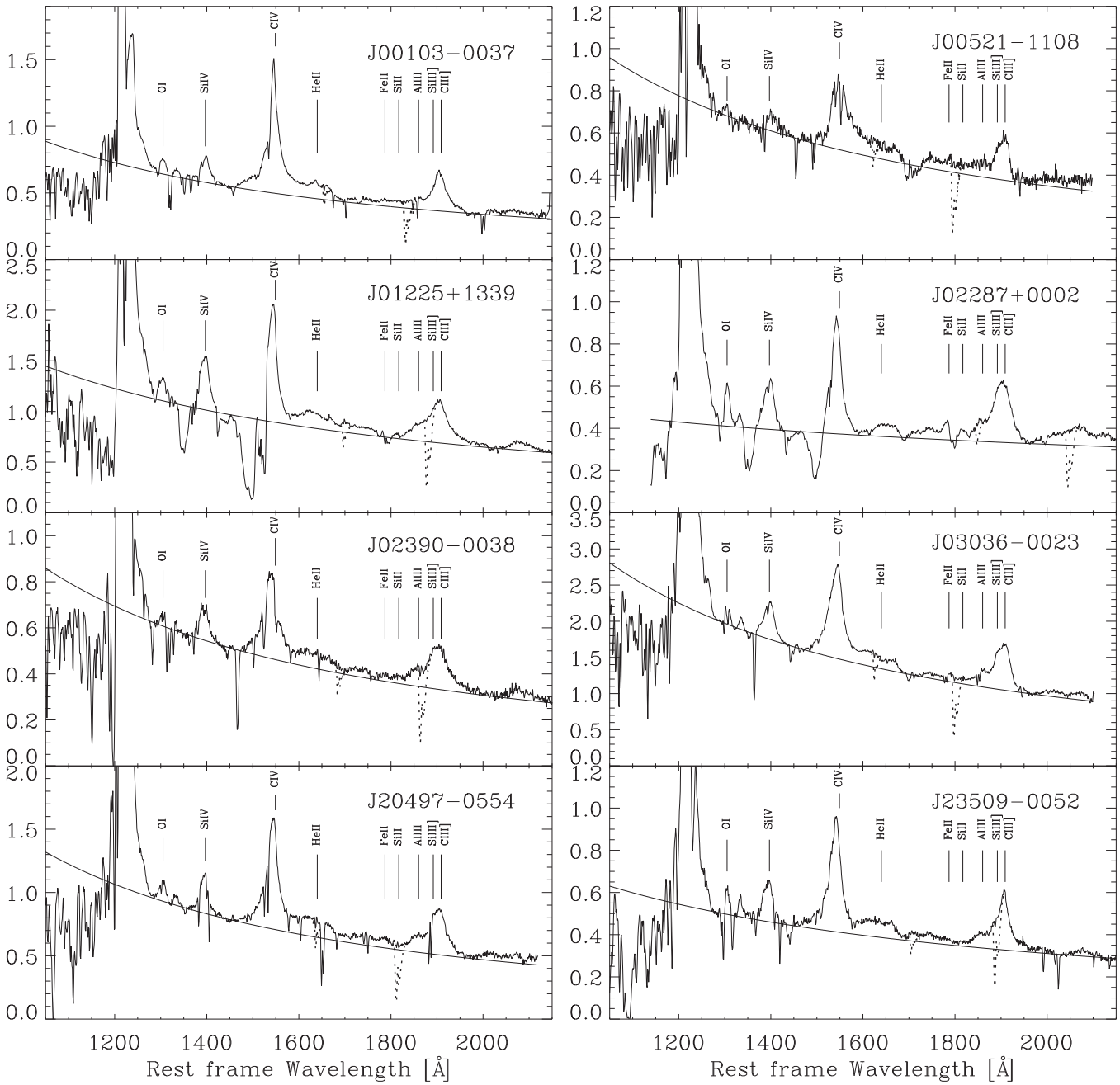

Figure 1. Sample of eight VLT spectra in rest frame wavelength. Abscissa is observed wavelength in Å, and ordinate is specific flux in units 10^{-14} erg s^{-1} cm^{-2} Å^{-1} corrected for Milky Way Galactic extinction. The superimposed dotted line is before atmospheric bands subtraction. We show the fitted continuum and the positions of the lines of our interest C III] λ1909 , Si III] λ1892, Al III λ1860, Si II λ1814, Fe II λ1787, C IV λ1549 and Si IV λ1397. J01225+1339 and J02287 are BAL quasars.

quasars. In our case no strong narrow lines are available, so we consider the peaks of Lyα, C IV λ1549 and C III] λ1909. The Lyα peak is affected by absorption and C IV λ1549 is an HIL feature often showing blueshifts and/or asymmetries (Gaskell 1982; Espey et al. 1989; Corbin 1990; Tytler & Fan 1992; Marziani et al. 1996; Richards et al. 2002; Baskin & Laor 2005; Sulentic et al. 2007). C III] λ1909 is blended with Si III] λ1892 and Fe III which is especially prominent in this region and could well affect the peak wavelength of the blend. This is especially true in Pop. A sources. Population B (Pop. B) sources show a rather weak Fe spectrum making the C III] λ1909 peak a more reliable z estimator.

Another option is to use the LIL O I λ1304 whenever it is strong. It is unfortunately blended with low ionization Si II λλ1304, 1309 ($^2P^0_{3/2,1/2}$–$^2S_{1/2}$). Both O I λ1304 and Si II λλ1304, 1309 are broad lines; however they are of low ionization and in both Pop. A and B their peak shifts with respect to rest frame should be consistent with Hβ or Fe II, and therefore rather modest, within a few hundred km s^{-1} (Sulentic et al. 2012; Marziani et al. 2013a). There is no hint of large systematic Hβ broad component (BC; where the BC represents the line core and will be defined in Section 4.3) peak shifts for all Pop. A sources (the majority in our sample) and ≈60% of Pop. B sources (Marziani et al. 2003a).

Photoionization simulations in the ($n_{\rm H}$, U) region of interest show O I λ1304 ≈ 2 Si II λλ1304, 1309, which is confirmed in the spectrum I Zw 1, where O I λ1304 and Si II λλ1304, 1309 are resolved. The two components of the Si II λλ1304, 1309 doublet

are set to the same intensity (i.e., we assume an optically thick case). We model the blend O I λ1304 + Si II λλ1304, 1309 with five Gaussians; the three components of the O I feature are produced by the Bowen florescence mechanism, and should show ratios consistent with their transition probabilities. Generating a model spectrum in IRAF (lines broadened to 4000 km s^{-1}) yields a rest frame peak wavelength of 1304.8 ± 0.2 Å (in vacuum), which we use as a reference for our VLT spectra. We also used He II λ1640 to check the rest frame assignment in the objects when it is clearly visible (J00103−0037, J00521−1108, J02287+0002, J02390−0038 and J23509−0052). Examination of Figure 1 reveals that the peak of O I λ1304 in source J00521−1108 is not observed clearly. We use C III] λ1909 to set the rest frame in this case. Redshifts obtained for three quasars, J01225+1339, J03036−0023 and J23509−0052, were obtained from O I λ1304, and are consistent with the redshift obtained with C III] λ1909. There are other sources J00103−0037, J02287+0002, J02390−0038, and J20497−0554 where the redshift estimation using both O I λ1304 and C III] λ1909 are not in good agreement (see Columns 3 and 4 of Table 1). The largest disagreement was found for J02287+0002, with $\Delta z \approx 0.0097$. In this case, the uncertainty is so large that it affects the interpretation of line profiles, and we are forced to repeat the line fitting with the assumption of two different redshifts.

Figure 1 shows the de-redshifted VLT-FORS1 spectra for our sample of eight quasars.

4. DATA ANALYSIS

4.1. Quasar Systematics

Quasar spectra are not all alike. There are significant differences in line intensity ratios and broad line profiles from object to object (Bachev et al. 2004; Marziani et al. 2010). More importantly, these differences can be organized in a systematic way (Boroson & Green 1992). Since the early 1990s several authors have stressed the importance of the E1 of quasars (e.g., Gaskell et al. 1999). Sulentic et al. (2000, 2007) expanded the E1 trends into a four-dimensional space involving optical, UV, and X-ray measures. They also defined spectral types along a sequence occupied by active galactic nucleus (AGN) in an optical plane involving Fe II and FWHM Hβ parameters (Sulentic et al. 2002). Objects at extreme ends of the E1 sequence are very different at almost all wavelengths and median spectra computed in spectral bins within this plane emphasize systematic changes in broad line properties (Sulentic et al. 2002, 2007). The most effective divider of the two quasar types appears to be at FWHM (H$\beta_{\rm BC}$) ≈ 4000 km s^{-1} for low-to-moderate luminosity sources (Marziani et al. 2009). The limit on FWHM corresponds to Eddington ratio $L/L_{\rm Edd} \sim 0.2 \pm 0.1$ (Marziani et al. 2003b).

Sulentic et al. (2002) gridded the BC of FWHM(H$\beta_{\rm BC}$) versus the $R_{\rm Fe\,II} = W({\rm Fe\,II}\ \lambda4570)/W({\rm H}\beta_{\rm BC})$ parameter plane into bins of fixed Δ FWHM = 4000 km s^{-1} and Δ $R_{\rm Fe\,II} = 0.5$. Quasar spectra in different bins are different in many measures. As mentioned earlier, the largest differences are found between NLSy1-like objects, Pop. A, and broader sources of Pop. B with FWHM(H$\beta_{\rm BC}$) $\gtrsim$ 4000 km s^{-1}.

Bins A1, A2, A3 are defined in terms of increasing Fe II λ4570 (see Figure 1 of Sulentic et al. 2002). Median composite UV spectra of low-z quasars were computed by Bachev et al. (2004). However, assignment to population and spectral type was originally done on the Hβ spectral range that was available for every source included in the composites. In the case of high redshift quasars, however, the Hβ spectral range is customarily not available. A proper analysis of the spectrum then requires sources to be assigned to either Pop. A or B, if not to a spectral type, from UV data alone. The two following criteria come from the analysis of optical lines profiles; previous work has shown that they can be applied to the UV lines as well.

1. *Broad line width*. The intermediate ionization lines Al III λ1860 and Si III] λ1892 are found to be equivalent to Hβ BC, with their FWHM in close agreement (Paper II). At high luminosity the limit FWHM = 4000 km s^{-1} must be increased to consider its dependence on luminosity. Following Marziani et al. (2009), we can set FWHM ≈ FWHM$_0$ $\left(L/10^{45}\right)^{1-\alpha/2}$ with FWHM$_0$ ≈ 4000 km s^{-1}. The limit should be considered as indicative because the value of a is not known with a high precision. However, high luminosity sources with FWHM $\lesssim$ 4000 km s^{-1} are found to be of Pop. A.
2. *Evidence of a prominent red wing indicative of a possible very broad component (VBC)*. Pop. B sources show C IV λ1549 profiles that resemble the Hβ ones (Marziani et al. 1996). A prominent redward asymmetry described by several authors (e.g., Wills et al. 1993; Corbin 1995; Punsly 2010; Marziani et al. 2010) is present in both C IV λ1549 and Hβ. This feature, if prominent, easily and uniquely identify Pop. B sources.

Two additional discriminating UV spectral properties include the following.

1. *C IV λ1549 equivalent width (EW)*. According to Bachev et al. (2004) there is a rather abrupt discontinuity in W(C IV λ1549) between spectral types A1 and A2, from ≈80 Å (A1) to ≈40 Å (A2). W(C IV λ1549) $\lesssim$ 40+2σ Å is a sufficient condition to identify a Pop. A source, albeit not a necessary one, as A1 sources do not satisfy this condition.
2. Prominence of Al III λ1860 and Si III] λ1892 with respect to C III] λ1909. The A3 and A4 spectral types show intensity ratios Al III λ1860/Si III] λ1892 $\gtrsim$ 0.5 and Si III] λ1892/C III] λ1909 $\gtrsim$ 1.

In addition, Pop. A sources show C IV λ1549 blueshift at half maximum intensity that are of larger amplitude than in Pop. B. However, not all Pop. A sources show blueshifts like most Pop. B sources (Sulentic et al. 2007). C IV λ1549 blueshifts are expected to be orientation dependent if the C IV λ1549 emitting gas is due to an outflow or wind (e.g., Flohic et al. 2012; Richards 2012, and references therein). A criterion based on C IV λ1549 blueshift will be useful only to identify and confirm the most extreme Pop. A sources, and will not be of general validity to distinguish Pop. A and B.

Previous and current work indicates that assignment to population is relatively straightforward for most sources (Bachev et al. 2004; Marziani et al. 2010; Sulentic et al. 2013; Sulentic et al. 2014). Some ambiguity may be present for sources right at the boundary between Pop. A and B (i.e., between spectral types A1 and B1).

4.2. Methodological Considerations on Multicomponent Fits

The SPECFIT IRAF task (Kriss 1994) allows us to fit the continuum, emission and absorption line components, Fe II and Fe III templates, and so on. We fit the emission lines in three spectral ranges: (1) 1340–1450 Å to model the 1400 Å blend most likely due to Si IV λ1397 and O IV] λ1402 (Wills & Netzer 1979), (2) 1450–1680 Å for analysis of C IV λ1549, and (3) 1750–2050 Å for analysis of the 1900 Å blend.

4.3. Line Components

We base our SPECFIT analysis on several previous observational results described in the previous Paper I and II, which point toward three different components in broad line profiles (see Marziani et al. 2010).

1. A BC showing a roughly symmetric profile with FWHM in the range 1000–5000 km s^{-1}. It is consistent with the component identified by Matsuoka et al. (2008). This BC dominates LILs in Balmer lines of Pop. A sources, while it becomes less prominent in Pop. B. The most relevant one is that Hβ can be described by a Lorentz function in Pop. A sources (Véron-Cetty et al. 2001; Sulentic et al. 2002), and by the sum of two Gaussians in Pop. B sources (a BC unshifted + a broader redshifted component, the VBC (e.g., Zamfir et al. 2010).
2. A VBC, as seen in LILs and HILs of most Pop. B sources, but is absent from Pop. A profiles. The VBC can be modeled as a Gaussian (FWHM $\sim$ 10000 km s^{-1}), often with a significant shift to the red. It can be called a defining property of Pop. B sources. This component is clearly identified in the C IV λ1549 line of Pop. B objects, and is also appreciable on the red side of C III] λ1909 of the Pop. B objects, J00103−0037 and J02390−0038, that are discussed in this paper.
3. A blueshifted broad component (BLUE), defined as the residual emission in the C IV λ1549 line after subtracting a scaled Hβ profile (Marziani et al. 2010). This BLUE component is often prominent in the C IV λ1549 and Lyα of Pop. A sources. It is much less intense in radio-loud Pop. B sources (Marziani et al. 1996; Punsly 2010; Richards et al. 2011). We model this profile as a blueshifted Gaussian. The Gaussian approximation is probably inappropriate especially if the BLUE component is strong—this component is believed to be produced in a partially obscured radial flow, not in a virialized emitting system.

Our multicomponent description of the broad line profile is rather crude as it involves mostly symmetric functions. While an unshifted symmetric function is expected for virial broadening, BLUE and the VBC are not necessarily Gaussian. A more accurate representation of BLUE may be obtained through a skew Gaussian. However, in the fitting of Hβ for Pop. B sources, two Gaussians provide a remarkably good fit in most objects and in median composites (Zamfir et al. 2010; Marziani et al. 2013b).

BLUE has been introduced because of the large blueshifted emission observed in C IV λ1549 of A3 and A4 sources—the large C IV λ1549/Hβ ratio on the blue side of the line profile clearly indicates different physical conditions than in the line core. The origin of BLUE may be ascribed to a predominantly radial outflow in a radiation driven wind context (e.g., Elvis 2000). A physically motivated definition of the VBC involves the ionization stratification that is likely found in Pop. B sources (as per echo mapping studies, e.g., Peterson & Wandel 1999)—because no significant VBC was detected in the Fe II blends even at the highest S/N, the VBC can be properly associated with the innermost BLR part where ionization is too high to allow for significant singly ionized iron emission. The VBC can account for the difference in full profile line width between Pop. B C IV λ1549 and Hβ. At the same time, if motion is predominantly virial, the VBC gas will respond first to continuum changes, as found in some reverberation studies (e.g., Peterson & Wandel 1999, who consider Pop. B sources). In (Paper II, Table 1) we tested whether our method yields results consistent with Hβ RM, but not with C IV λ1549 RM.

We then use the results of Marziani et al. (2010) and Paper II—the BC of the Si III] λ1892, Al III λ1860 and C IV λ1549 lines is similar to that of Hβ, including the FWHM and profile shape, either Gaussian or Lorentzian. The similarity helps us define whether an object is Pop. A or B in this paper. We use the BC (and not the full line) intensity to compute the line ratios considered in our method (Section 7.1).

Baldwin et al. (1996) presented a similar analysis. Their Figure 2 organizes spectra in a sequence that is roughly corresponding to E1, going from Al III λ1860-strong sources to objects whose spectra show prominent C III] λ1909 along with weak Al III λ1860 (Bachev et al. 2004). Two of the three line components they isolated correspond to those we consider in this paper: a blue-shifted feature, and a more symmetric, unshifted, and relatively narrow component (NC) that we call LIL-BC. Less obvious is the correspondence of a third feature, although it appears to be the redshifted part of what we call the VBC.

4.4. Fe II and Fe III Emission

Fe II emission is not strong in the spectral range we studied. Significant Fe III emission is however expected close and underlying the 1900 Å blend, especially for Pop. A sources (Francis et al. 1991; Vanden Berk et al. 2001). Our approach is completely empirical and employs an Fe II + Fe III template taken from templates successfully used in Paper I (Section 3.2 provides more details) and Paper II. We adopt an Fe II template that is based on a CLOUDY simulation and is not very far from the preferred model of Brühweiler & Verner (2008), and the Fe III template of Vestergaard & Wilkes (2001). The Fe II intensity scale of the template is anchored to the Fe II UV 191 multiplet intensity, although we repeat that Fe II is in general weak. This allows us to reliably constrain Fe II emission underlying C IV λ1549 and the 1900 Å blend. Similarly, the Fe III intensity is set by a feature external to the 1900 Å blend (2080 Å).

4.5. Expected Emission from the Three Components

We looked for evidence of three possible components, as described above: BC and BLUE component for Pop. A, and BC, BLUE, and VBC for Pop. B sources. The three components show different strengths in different lines, and are negligible in some lines, which simplifies the interpretation of blended features.

4.5.1. Pop. A

The C IV λ1549 and He II λ1640 are modeled assuming that a BC and a BLUE component is present in both lines. The BC and BLUE component of He II λ1640 account for the flat shape of the broad He II λ1640 emission on the red side of C IV λ1549.

The 1400 Å blend is modeled assuming a single BC and a BLUE component similar to those of C IV λ1549. Because O IV] λ1402 and Si IV λ1397 are inextricably blended together, we consider the total blend flux for metallicity analysis (Section 6.3). However, high-density gas should emit negligible intercombination O IV] λ1402. In the extreme Pop. A sources, the BC could be ascribed to mainly Si IV λ1397, while the BLUE component is a blend of both Si IV λ1397 and O IV] λ1402. In those cases, the Si IV λ1397 + O IV] λ1402 blend closely resembles the shape of C IV λ1549.

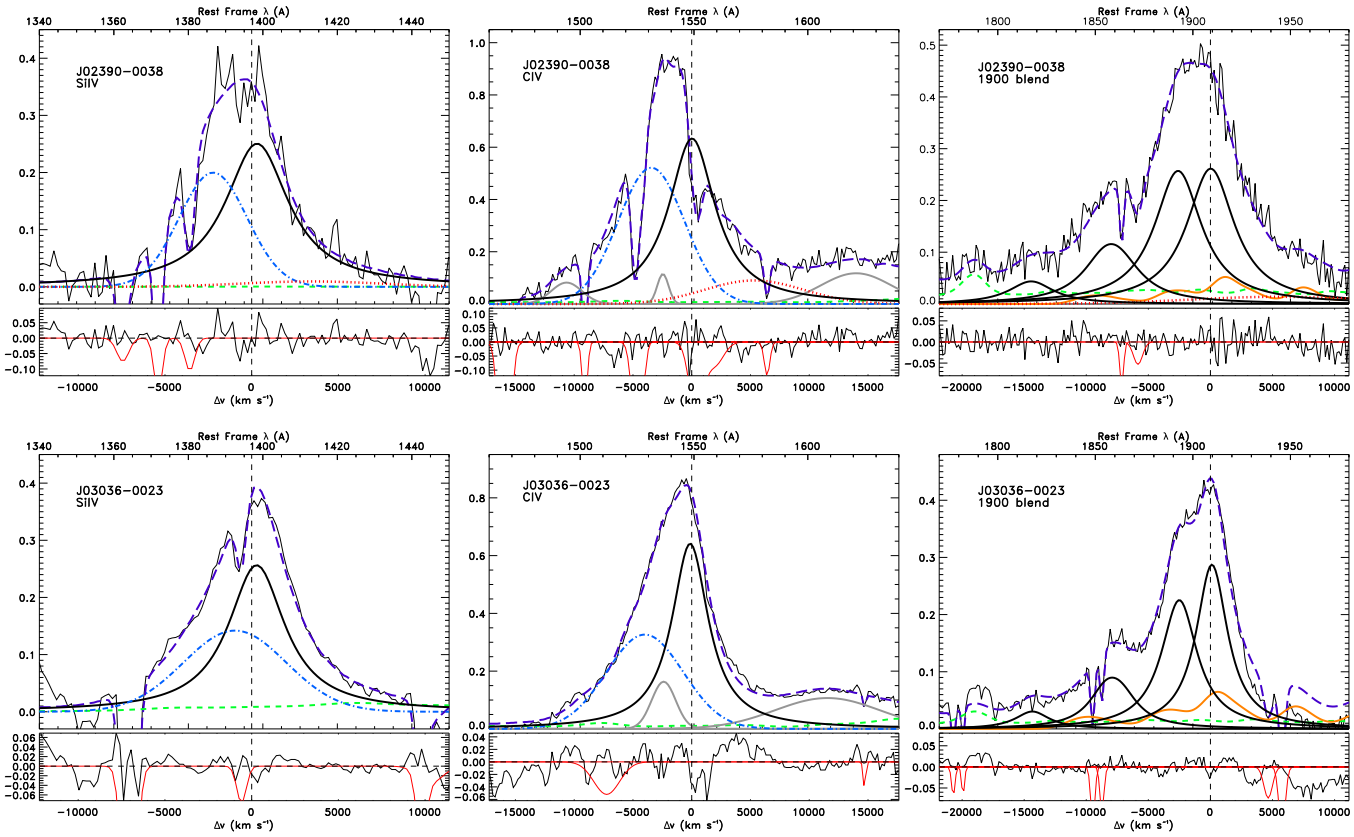

Figure 2. Fits for Pop. A objects: J02390−0038, J03036−0023, J20497−0554, and J23509−0052. Upper panels show the fits and the lower panels under the fits show the residuals and also the fitted absorptions lines shown in red. Upper abscissa is the rest frame wavelength in Å, lower abscissa is in velocity units, and ordinate is specific flux in arbitrary units. Vertical dashed line is the rest frame for C IV λ1549 and C III] λ1909. Purple long dashed line is the fit, solid black lines are the BCs: Si IV λ1397 in left panels, C IV λ1549 in center panels, and C III] λ1909 , Si III] λ1892, Al III λ1860, Si II λ1814 in right panels. For Al III λ1860 we show the sum of the doublet. Short green dashed line is Fe II. Fe III is shown in orange dash-triple-dot line in the right panels. Blue dash-dot line in the left and center panels is the blueshifted component of Si IV λ1397 and C IV λ1549 respectively. Dotted red line is the VBC, which is also present in C III] λ1909 for Pop. B objects. In the center panels we show with gray lines the contribution of N IV λ1486, Si II λ1533 and He II λ1640 core and blueshifted components.

(A color version of this figure is available in the online journal.)

We expect that the Al III λ1860 doublet is emitted exclusively in the BC, the region where Fe II is also emitted. This is empirically confirmed by the aspect of the 1900 Å blend in many sources, where we do not see any evidence of BLUE or VBC in Al III λ1860. We remark that the Al III λ1860 doublet is relatively unblended, and that a BLUE feature as strong as in the C IV λ1549 profile of Pop. A sources would not easily escape visual detection. The same is also true for Si III] λ1892. Several fits that included a BLUE component in C III] λ1909 yielded zero intensity, implying a large C IV λ1549/C III] λ1909 (Marziani et al. 2010).

The BLUE component is very weak or undetectable in the vast majority of the Hβ profiles analyzed in Marziani et al. 2003a (but see Zamfir et al. 2010 for several cases of Hβ BLUE), whereas it is prominent in Lyα; the Lyα/Hβ ratio in this component is high. In summary, the BLUE component is visually strong in Lyα and C IV λ1549. A He II λ1640 BLUE component is needed for a self-consistent fit of the C IV λ1549+He II λ1640 blend.

Because the shift and FWHM are assumed to be the same for all lines (and templates) in the 1900 Å blend, the only free parameters in addition to shift and FWHM are the intensities of the six components: two from the templates, Si II λ1814 and Al III λ1860 that are not heavily blended, and Si III] λ1892 and C III] λ1909. The SPECFIT analysis is especially helpful to measure in a non-subjective way and taking all constraints into account, the two parameters that are most affected by blending: the intensity of Si III] λ1892 and C III] λ1909 (any Fe III λ1914 contribution in excess to that of the adopted template is included in the estimated C III] λ1909 intensity).

4.5.2. Pop. B

As pointed out by Marziani et al. (2010) the plateau appearance of the far red wing of C IV λ1549 is accounted for a BLUE component and a redshifted VBC of He II λ1640, whose shifts and widths match those of C IV λ1549.

The 1400 Å blend is fit with a single BLUE, BC, and VBC. The VBC is rather faint (left panels of Figures 2–4), allowing for an estimate of the BC. However, considering that the blend is due to five components of O IV] λ1402 and two of Si IV λ1397, whose relative intensities are unknown, so we again consider the total blend flux for metallicity analysis (Section 6.3).

No VBC emission is observed (or expected) in Al III λ1860, Fe III or Fe II. These constraints also help to make the fits less ambiguous. However, the presence of a VBC in C III] λ1909 and Si III] λ1892 complicates the fit of the 1900 Å blend. In any case, considering that we can expect the VBC to be fitted with a shifted Gaussian with FWHM $\sim$ 10,000 km s^{-1}, the unblended part of the C III] λ1909 VBC provides a strong constraint. Considering that the wavelength separation between Si III] λ1892 and C III] λ1909 is $\approx$3000 km s^{-1}, $\ll$ FWHM VBC, what we model is most likely blended Si III] λ1892 and C III] λ1909 VBC emission.

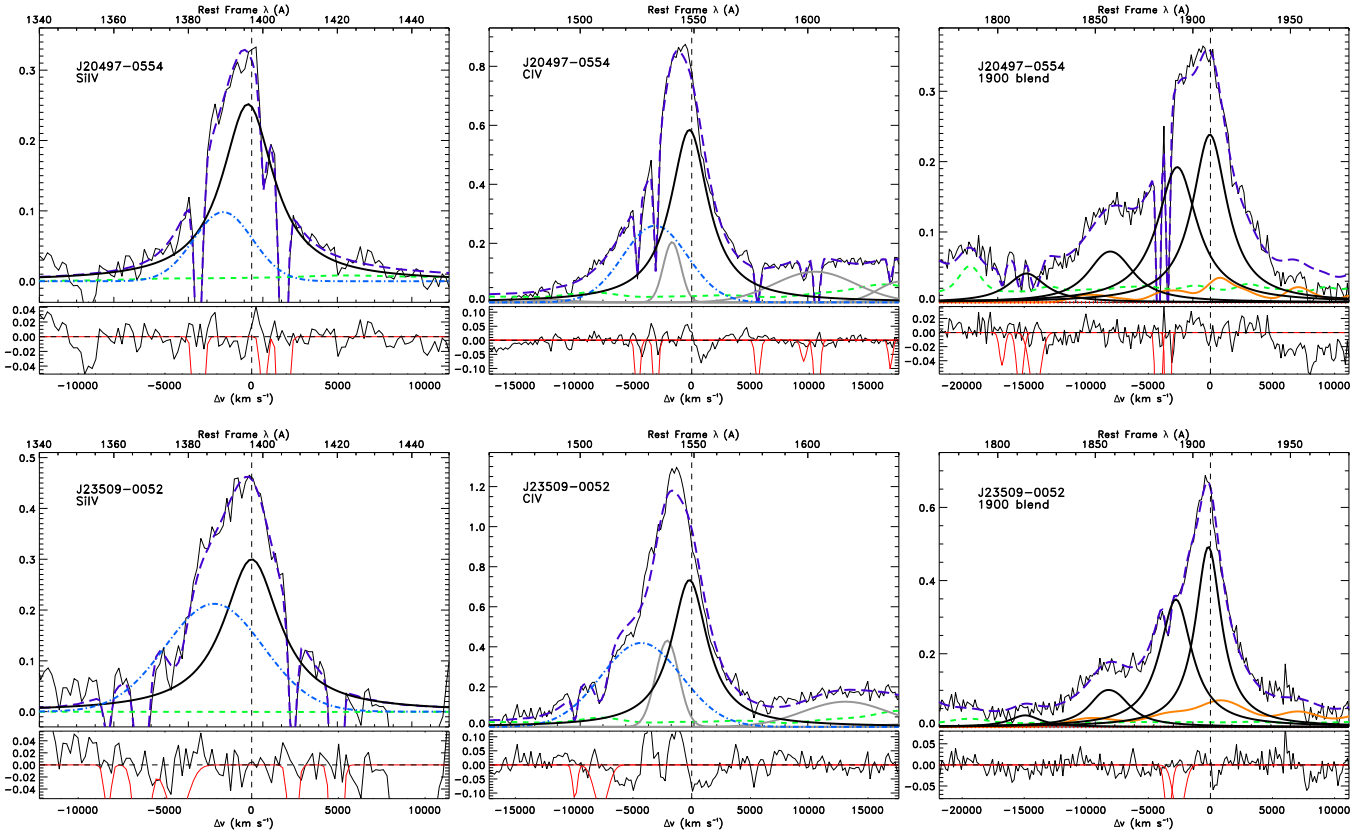

Figure 2. (Continued)

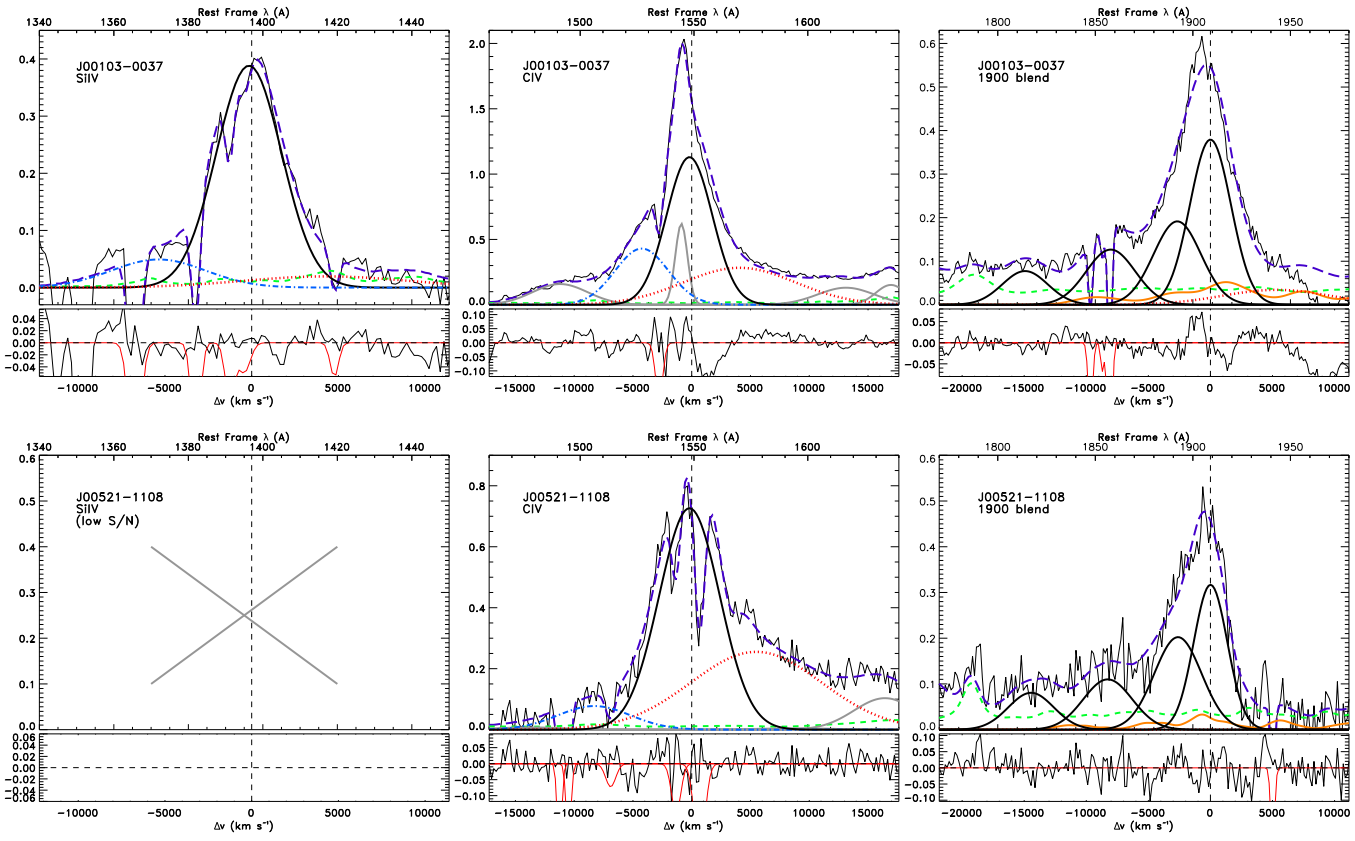

Figure 3. Fits for Pop. B objects: up J00103−0037 and low J00521−1108. Units and meaning of symbols are the same of Figure 2.
(A color version of this figure is available in the online journal.)

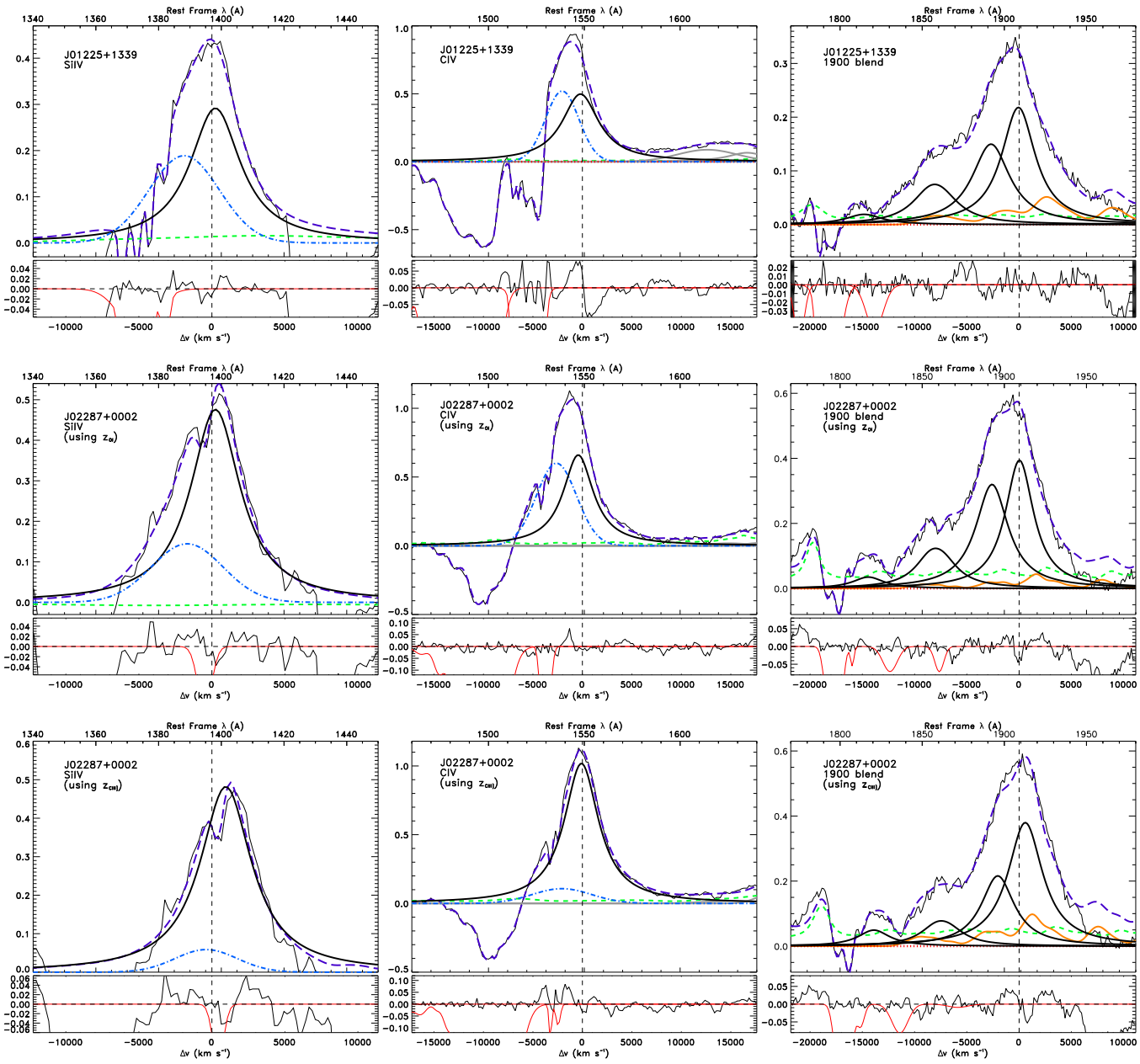

Figure 4. Fits for BAL quasars: up J01225+1339, middle J02287+0002 using $z_{O\,I\,\lambda1304}$ rest frame, and low J02287+0002 using $z_{C\,III\,\lambda1909}$ rest frame. Note in J02287+0002 the line displacement with the consequently line intensity changes, specially in C III] λ1909 , Si III] λ1892 and C IV λ1549 broad and blueshifted components. Units and symbols are the same as in Figure 2.

(A color version of this figure is available in the online journal.)

4.6. Absorption Lines

We also fit absorption broad and narrow lines when they were needed in the SPECFIT routine, along with the emission line components described above. Absorption lines were modeled with a Gaussian profile. Initial guesses were provided to SPECFIT from measurements of the EW, centroid, and FWHM obtained interactively with the IRAF task SPLOT. In the BAL cases, we fitted first a single broad absorption line and, looking at the residuals, we added smaller absorption lines to fill the trough. The fitted absorption lines are shown in red in the lower panels of Figures 2–4. Details on absorption features are given in the discussion of individual sources (Section 5). Errors introduced by the absorption lines are analyzed in the following section.

4.7. Errors

Apart from the effect of noise, which is treated as statistical source of error, we identify five main sources of error that may significantly affect our measures.

1. A and B atmospheric band correction (already described in Section 3.1). The most serious effect is when the A/B band overlaps Si II λ1814.
2. Line profile shape, Gaussian or Lorentzian (Pop. A or B). The distinction between Pop. A and B is based on line width with the boundary at FWHM Hβ $\approx$ 4000 km s^{-1} in low luminosity quasars and around $\approx$5000 km s^{-1} at higher luminosity, such as the eight sources presented here. Most of our quasars are unambiguously Pop. A or B because of line width and because Pop. B sources show

an Hβ VBC, while Pop. A sources have a prominent C IV λ1549 BLUE component. In these cases, only one profile shape (Gaussian or Lorentzian) was fitted. In the case of the borderline objects marked in Column 6 of Table 6 (J01225+1339, J02287+0002, J02390−0038) we made two different fits, using Gaussian and Lorentzian line profile shapes. A posteriori, we can say that the estimated line ratios are rather insensitive to the emission component profile shape—assuming a Gaussian or Lorentzian profile yields the same ratio for the strongest lines (i.e., C IV λ1549, Si III] λ1892, Al III λ1860) upon which our analysis is based (with an uncertainty of $\sim$10%).

3. Rest frame determination using O I λ1304 or C III] λ1909. In some cases the redshift estimates derived from the two lines do not agree, most likely because of absorptions present in O I λ1304 and because this is not a very intense line. The principal affect of uncertainty in the rest frame placement is the estimation of the peak wavelength of C IV λ1549. If the line peak differs from λ1549 Å, the BC intensity is diminished and we infer a greater contribution from the BLUE component. Similarly, for the blend 1900 Å, the rest frame shift may increase or decrease our estimate for the strength of C III] λ1909 with consequent decrease or increase of the Si III] λ1892 contribution. This additional source of uncertainty affects J02287+0002, J02390−0038, and J20497−0554. However, only in the case of J02287+0002 the redshift difference produces a significant effect due to a $\Delta z \approx 0.0097$ (Table 1). For those three cases we made two different fits, one for each z.
4. Fe II intensity (continuum placement). Broad Fe II emission can produce a pseudo-continuum affecting our estimates of emission line intensities. Si II λ1814 is especially affected in our spectra because it is weak. Al III λ1860 is similarly affected when it is weak. The effect is less noticeable for C IV λ1549 because expected Fe II emission underlying the C IV λ1549 line is also weak for strong Fe II emitters. The Fe III (UV34) and Fe II emission is not very strong and a posteriori we find that there is no significant effect, with the exception of Si II λ1814 measures, but the uncertainty can be included in the one associated with continuum placement that contributes to the statistical error. For all the objects, we made two extra fits considering an upper and a lower continuum limit, as described in Paper I.
5. BALs principally affect the blue side of C IV λ1549. We also find an absorption feature between Fe II λ1787 and Si II λ1814 (eg., Figure 4). In sources J01225+1339 and J02287+0002, the derived line intensities should be viewed with caution, because we fit unabsorbed components where the total flux eaten by absorptions is unknown.

In the case of C III] λ1909 we need to consider the possibility that the profile is narrower because there might be a contribution from different regions; indeed, the SPECFIT routine usually converges toward a narrower profile if the C III] λ1909 width is not constrained. The effect depends on the strength of the Fe III λ 1914 feature, which is expected to be prominent only in extreme Pop. A sources (Paper I). These sources of uncertainty are included, when appropriate, in the errors reported in Table 2. However, from the above considerations it is clear that a faint line like Si II λ1814 can be used mainly for confirmatory purposes because of the large errors plaguing its intensity estimates.

Finally, we note that the errors derived from the SPECFIT task are much smaller than the errors reported here. The reason is that the errors reported by the tasks are formal errors associated with the multicomponent fit only.

4.7.1. Effect of Absorption Lines on Multicomponent Fits of Blended Emission Lines

Several emission features profiles are affected by significant absorptions. In the case of the two BAL QSOs, the BLUE component of C IV λ1549 is affected in a way that is very difficult to quantify since we do not know a priori its shape. We do not assign an error to the BLUE fluxes reported in Table 2. The fit obtained following our standard procedure provides a value that could be considered an approximate lower limit (there are no constraints setting the flux removed from the emission component by the BALs). We do not, however, make use of the blue shifted component measurements in the analysis of the data for either the BALs or the other sources. Any effect on the BC is instead of direct relevance to the $r_{\rm BLR}$ computations presented in this paper. The sources most affected by absorptions are the two BAL QSOs J01225+1339 and J02287+0002 (for both O I λ1304 and C III] λ1909 rest frames), J00521−1108 (whose C IV λ1549 line core is eaten by narrow absorption lines), and J02390−0038 (whose C IV λ1549 blue side C IV λ1549 is significantly affected). Narrow absorptions also affect the Al III λ1860 profile of J03036−0023.

We analyzed the behavior of χ^2_ν[25] changing the BC intensity at fixed steps starting from the best fit, and leaving all other components free to vary. For C IV λ1549 we leave the BLUE and the VBC (if present) components and absorptions free to vary; for the case of the 1900 Å blend, we leave C III] λ1909, Si III] λ1892 and Si II λ1814 free to vary, with the BC of C IV λ1549, Al III λ1860 and the continuum placement fixed at the "best fit" value (the ones of the Table 2). Subsequently, we vary the BC of C IV λ1549 and Al III λ1860 intensities at fixed steps starting from the best fit. We measured the χ^2_ν of each fit and plotted $\chi^2_\nu/\chi^2_{\nu,\rm min}$ versus BC intensity (we show the cases of J02287+0002$z_{\rm O\,I}$ and J00521−1108) in Figure 5. We found that the errors given in Table 2 are always larger than those from this analysis. We conclude that the C IV λ1549 BC is only slightly affected by the degeneracy in the absorption/emission on the blue side of the C IV λ1549 profile. This was expected because the BC is assumed symmetric, constrained by the red side of the C IV λ1549 profile, and is not affected by broad absorptions. The only case that is influenced by narrow/semi-broad absorption is J00521−1108, where the absorptions cluster around the systematic velocity of the quasar, making it apparently more difficult to unambiguously constrain the C IV λ1549 BC intensity. However, even in this case, the behavior of the χ^2_ν indicates that the uncertainties are still below the ones obtained propagating the errors associated with the multicomponent fits and the other sources of errors. The confidence limit obtained from the behavior of the χ^2_ν is $\pm$1.4 at 1σ. In one case (J00103−0037) the Al III λ1860 line appears to be significantly affected by absorption lines, and we applied the same procedure to estimate the effect of the absorptions, obtaining $\pm$0.3 at 1σ.

5. RESULTS OF LINE COMPONENT ANALYSIS ON INDIVIDUAL OBJECTS

In Figures 2–4, we show our best fits for the VLT sample taking into account the considerations reported in Section 4.

[5] χ^2_ν is the normalized χ^2 for degrees of freedom $\nu \approx 100$ (Bevington 1969).

Table 2
Line Fluxes[a]

Object	C III] λ1909		Si III] λ1892	Al III λ1860	Si II λ1814	C IV λ1549			Si IV λ1397+O IV] λ1402		
	BC	VBC				BC	BLUE	VBC	BC	BLUE	VBC
J00103−0037	5.0 ± 2.1	1.2 ± 1.4*	2.9 ± 1.0	2.0 ± 0.8	1.1 ± 0.8:	14.3 ± 8.3	6.3 ± 1.8	8.7 ± 2.4	4.3 ± 2.4	0.8 ± 1.5	0.5 ± 0.9
J00521−1108	3.1 ± 0.4	0.0 ± 0.1*	2.8 ± 0.7	1.6 ± 0.9	1.1 ± 0.9	12.6 ± 3.3	1.3 ± 1.3	6.8 ± 3.1	...	...	...
J01225+1339	10.7 ± 1.4	...	8.3 ± 1.3	4.4 ± 2.1	1.0 ± 1.0	22.7 ± 6.0	14.2 :	...	11.2 ± 2.9	6.7 ± 1.9	...
J02287+0002 (1)	6.5 ± 2.0	...	6.0 ± 2.2	2.5 ± 1.1	0.6 ± 0.7	11.0 ± 5.2	7.4:	...	7.2 ± 3.4	2.1 ± 1.3	...
J02287+0002 (2)	7.7 ± 2.0	...	4.2 ± 2.2	1.6 ± 1.1	0.9 ± 0.7	17.4 ± 11.2	2.1:	...	7.5 ± 3.4	0.7 ± 1.3	...
J02390−0038	4.8 ± 1.3	0.6 ± 1.0*	4.7 ± 1.2	2.2 ± 0.6	0.8 ± 0.7	9.8 ± 2.4	7.6 ± 1.2	2.0 ± 1.3	3.2 ± 0.7	1.8 ± 0.8	0.2 ± 0.3
J03036−0023	13.2 ± 1.1	...	11.8 ± 1.2	5.2 ± 1.5	1.5 ± 1.2 :	29.5 ± 3.5	20.6 ± 3.3	...	11.1 ± 1.9	7.4 ± 2.4	...
J20497−0554	8.0 ± 1.1	...	7.4 ± 0.6	3.0 ± 1.3	1.5 ± 1.5 :	18.4 ± 2.2	9.2 ± 2.2	...	6.6 ± 2.5	2.0 ± 1.1	...
J23509−0052	5.2 ± 1.2	...	4.6 ± 1.6	1.5 ± 0.5	0.4 ± 0.4	9.2 ± 1.2	7.8 ± 2.4	...	3.6 ± 1.5	2.9 ± 1.3	...

Notes. [a] Units are 10^{-14} erg s^{-1} cm^{-2} Å^{-1}. (1) Considering $z_{\rm O\,I}$. (2) Considering $z_{\rm C\,III}$. (:) approximated values. In Si II λ1814, the line is affected by telluric absorptions. In the C IV λ1549 line, the BLUE component is affected by BALs (see Figure 1). We do not measure Si IV λ1397 for J00521−1108 because they have low S/N. (*) Consistent with no emission.

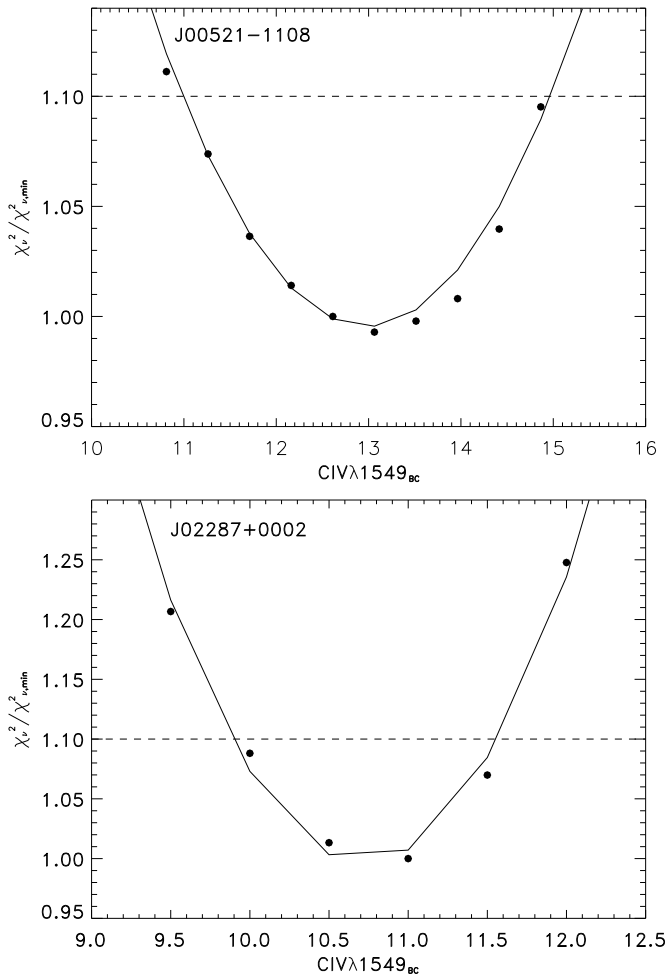

Figure 5. Behavior of χ^2_ν as a function of C IV λ1549$_{\rm BC}$ intensity for the fit of J00521−1108 (top) and of J02287+0002($z_{\rm O\,I}$) (bottom). Abscissa is the ratio $\chi^2_\nu/\chi^2_{\nu,\rm min}$, ordinate is the C IV λ1549$_{\rm BC}$ intensity given in Table 2. The continuous line is a polynomial fit of order 2, and the dashed line identifies the $\chi^2_\nu/\chi^2_{\nu,\rm min}$ at 1σ confidence level.

In the left panels we present the fits for the Si IV λ1397 line, the center panels are for the C IV λ1549 line, and the right panels are for the 1900 Å blend. The fluxes and equivalent widths are in Tables 2 and 3. Table 4 shows the weak lines around C IV λ1549. For the C IV λ1549 and Si IV λ1397 lines, we show the BC, BLUE, and VBC. Errors are at a 2σ confidence level and include the sources of uncertainty described in Section 4.7. Errors are then quadratically propagated according to standard practice to compute intensity ratios and their logarithm.

We present in the following a phenomenological description of the fits.

5.1. Pop. A Objects

We show the fits for our four Pop. A objects in Figure 2.

1. *J02390−0038*. This object is borderline because FWHM(BC) ∼ 4600 km s^{-1} places it close to the boundary between Pop. A and Pop. B, at high L. In support of the Pop. B assignment we note that the C IV λ1549 profile is best fitted assuming a VBC emitting region. In addition, we find Fe II λ1787 to be weaker than Si II λ1814. On the other hand, C III] λ1909 is flat topped, has a very similar intensity as Si III] λ1892 and the blend is best fitted using Lorentzian profiles. This object shows a very strong BLUE component in C IV λ1549 that is also indicative of a Pop. A source. Si IV λ1397 has a similar flat topped profile as in C III] λ1909 and probably as in C IV λ1549. We fit the Si IV λ1397 + O IV] λ1402 blend following the C IV λ1549 fit. As the strongest and less ambiguous features indicate Pop. A, we assign this object to Pop. A and use Lorentzian profiles to fit the BCs.
2. *J03036−0023*. We estimate for this source an FWHM(BC) ∼ 3700 km s^{-1} and we use a Lorentzian function to fit the BCs. The peak of C IV λ1549 is blueshifted and requires a strong BLUE component. The bump on the red side of C IV λ1549 can be accounted for by He II λ1640 BC and BLUE components. There is no evidence for a redshifted component in C III] λ1909. Al III λ1860 is prominent. Unfortunately the blue wing of Si II λ1814 and the red wing of Fe II λ1787 are affected by A-band absorption.
3. *J20497−0554*. This source shows FWHM(BC) ∼ 3800 km s^{-1}. As for J03036−0023, the C IV λ1549 line can be accounted for by an unshifted BC (assumed Lorentzian) and a considerable contribution of a BLUE component. We see a prominent Al III λ1860 line and Fe II λ1787. Si III] λ1892 is affected by several narrow absorption lines; however, it is obviously strong. The lack of a red wing on C III] λ1909 suggests that no VBC is present. There are several absorption lines in the wings of Si IV λ1397. However, the line profile can be extrapolated over them.

Table 3
Equivalent Widths

Object	C III] λ1909 $_{BC}$	C III] λ1909 $_{Tot}$	Si III] λ1892	Al III λ1860	Si II λ1814	C IV λ1549$_{BC}$	C IV λ1549$_{Tot}$	(Si IV λ1397+O IV] λ1402)$_{BC}$	(Si IV λ1397+O IV] λ1402)$_{Tot}$
J00103−0037	13.7 ± 5.8	17.1 ± 7.2	7.9 ± 3.0	5.3 ± 2.8	2.9 ± 2.5 :	29.0 ± 16.1	59.6 ± 18.0	7.4 ± 4.3	9.7 ± 6.7
J00521−1108	8.2 ± 1.5	8.2 ± 2.4	7.3 ± 2.5	4.0 ± 2.6	2.6 ± 2.1	24.2 ± 13.4	40.1 ± 15.8	...	...
J01225+1339	15.3 ± 3.5	...	11.6 ± 3.1	6.0 ± 3.6	1.4 ± 1.6	25.5 ± 9.1	41.6 ± 9.7	11.1 ± 3.9	17.7 ± 4.7
J02287+0002[(1)]	19.3 ± 6.7	...	17.8 ± 5.7	7.4 ± 3.8	1.8 ± 2.2	28.9 ± 8.7	48.0 ± 20.5	18.8 ± 6.0	24.3 ± 6.7
J02287+0002[(2)]	22.8 ± 6.7	...	12.3 ± 5.7	4.7 ± 3.8	2.6 ± 2.2	48.2 ± 9.6	54.0 ± 24.6	18.8 ± 6.0	20.7 ± 6.7
J02390−0038	14.5 ± 4.1	16.5 ± 5.3	13.9 ± 3.7	6.4 ± 2.2	2.1 ± 1.7	21.3 ± 5.6	42.2 ± 7.3	6.0 ± 1.5	9.7 ± 3.7
J03036−0023	12.4 ± 1.8	...	10.9 ± 1.8	4.6 ± 1.6	1.3 ± 1.1 :	19.7 ± 3.7	33.3 ± 4.8	6.4 ± 1.5	10.7 ± 2.9
J20497−0554	15.5 ± 3.5	...	14.1 ± 2.3	5.6 ± 2.9	2.7 ± 2.5 :	25.4 ± 5.6	38.1 ± 7.1	8.0 ± 3.7	10.3 ± 4.0
J23509−0052	15.8 ± 4.0	...	13.7 ± 5.3	4.4 ± 1.8	1.1 ± 0.9	22.0 ± 4.2	40.5 ± 10.6	7.7 ± 3.7	14.0 ± 5.1

Notes. (1) Considering $z_{O\,I}$. (2) Considering $z_{C\,III}$. (:) Si II λ1814 approximated values due to the line are affected by telluric absorptions.

Table 4
Weak Lines around C IV λ1549[a]

Object	N IV] λ1486	Si II λ1533	He II λ1640	
			BC	BLUE
J00103−0037	2.4 ± 1.9	1.1 ± 0.8	1.3 ± 0.4	2.0 ± 1.8
J00521−1108	0.1 ± 0.2	0.1 ± 0.7	2.4 ± 1.2	0.1 ± 0.2
J01225+1339	...	1.0 ± 1.8	3.2 ± 3.4	4.3 ± 1.8
J02287+0002(1)	...	...	0.1 ± 0.3	1.2 ± 0.9
J02287+0002(2)	...	...	0.6 ± 0.4	0.4 ± 0.2
J02390−0038	0.6 ± 0.7	0.3 ± 1.0	0.0 ± 0.4	1.8 ± 0.9
J03036−0023	...	1.5 ± 1.2	0.5 ± 0.5	9.2 ± 3.4
J20497−0554	0.3 ± 0.6	1.5 ± 1.5	1.8 ± 0.8	4.6 ± 2.7
J23509−0052	...	0.4 ± 0.4	0.2 ± 0.9	2.5 ± 1.6

Notes. [a] Units are 10^{-14} erg s^{-1} cm^{-2} Å^{-1}. (1) Considering $z_{\rm O\,I}$. (2) Considering $z_{\rm C\,III]}$. We do not show He II $\lambda 1640_{\rm VBC}$ because is very weak when is considered.

4. *J23509−0052*. This source has FWHM(BC) ∼3600 km s^{-1}. C IV λ1549 shows a slight blue asymmetry with a BLUE component required to model it. The contribution of Fe II is small and Fe II λ1787 is weak. C III] λ1909 is very strong. Al III λ1860 is affected by A-band absorption; the profile we fit is probably an upper limit. This object could well belong to spectral type A1 that includes Pop. A sources with the lowest $R_{\rm Fe\,II}(\lesssim 0.5)$. Five absorption lines affect the Si IV λ1397 + O IV] λ1402 blend, but luckily they do not affect the core of the blend.

5.2. Pop. B Objects

1. *J00103−0037*. This source has an FWHM(BC) ∼ 4500 km s^{-1}. The red side of C IV λ1549 is blended with He II λ1640. Fitting a BC with no shift plus a BLUE component to C IV λ1549 leaves a very large residual on the red side. A redshifted VBC is needed to model the spectrum (Figure 3, upper center). The faint narrow line under C IV λ1549 can be explained as the NC of C IV λ1549 (see Sulentic et al. 2007). The presence of a similar NC in C III] λ1909 could potentially explain the large residual seen ∼1900 Å. We specifically note the prominent C III] λ1909 emission and weak (but well detected) Al III λ1860 (Figure 3, upper right). Two narrow absorption lines are superimposed on the Al III λ1860 profile. Their wavelength, FWHM, and EW are 1847 Å, 430 km s^{-1} and 0.49 Å, respectively, for the one on the blue side, and 1857 Å, 400 km s^{-1} and 0.94 Å for the other on the red side. These absorption lines, being narrow and of low EW, do not affect the uncertainty in the Al III λ1860 measure. The Fe II "bump" at 1787 Å (UV 191) is appreciable. Fainter Fe II emission is relatively unimportant because Fe II creates a pseudo-continuum. Si II λ1814 is compromised by A-band absorption. The blend at 1900 Å includes a C III] λ1909 VBC and the fit indicates C IV λ1549/C III] λ1909 (VBC) ≈ 7, which is reasonable. We found several absorption lines on the blue side of the Si IV λ1397 + O IV] λ1402 blend (Figure 3, upper left), which significantly affects its BLUE component, which seems at any rate to be fainter than the one of C IV λ1549.
2. *J00521−1108*. This source shows the noisiest spectrum in the sample. We fit an FWHM(BC) ∼ 5300 km s^{-1} with C IV λ1549 requiring a large VBC to account for the red wing (Figure 3, lower center). Absorption features seriously affect the C IV λ1549 profile—we fit three Gaussian absorptions with lambda, FWHM, EW: (1) 1542 Å, 1050 km s^{-1} and 0.93 Å, (2) 1552 Å, 1150 km s^{-1} and 1.79 Å, and 3) 1564 Å, 1800 km s^{-1} and 0.88 Å. The profile of C III] λ1909 is strongly asymmetric due to some sort of absorption on the red side. Al III λ1860 is weak and consistent with Pop. B (Figure 3, lower right). We decide not to carry out a fit of the Si IV λ1397 + O IV] λ1402 blend because it is too noisy.

5.3. BAL QSOs

We fit our two BAL quasars using Lorentzian profiles following Sulentic et al. (2006a). Note that the identification of C III] λ1909 in the BAL quasars and in sources with strong Al III λ1860 is debatable (Hartig & Baldwin 1986), as strong Fe III λ1914 could take the place of most C III] λ1909 emission.

1. *J01225+1339*. C IV λ1549 is highly affected by two broad absorption lines (Figure 4, upper center) with blueshifts of 5200 and 10,800 km s^{-1} at peak absorption with equivalent widths/FWHM −12 Å/3900 km s^{-1} and −25 Å/5200 km s^{-1}, respectively. The starting and terminal velocities of the trough range from −3800 to −17,000 km s^{-1}. The blueshift of the C IV λ1549 peak leads us to suspect a large BLUE emission component. The 1900 Å blend shows absorptions coincident with Fe II λ1787 and the blue side of Si II λ1814 which is unambiguously detected (Figure 4, upper right). Al III λ1860 is prominent, which implies that this a Pop. A source. The FWHM(BC) ∼ 4400 km s^{-1} is consistent with a high-luminosity Pop. A source. It is also possible that this BAL quasar is an outlier like Mark 231 at low-z (Sulentic et al. 2006b), in other words an extreme Pop. A object. The C III] λ1909 is well fitted with a Lorentzian profile. Broad A band atmospheric absorption lies over Si III] λ1892. The 1400 Å blend is also affected by two broad absorption lines on both sides of the line (Figure 4, upper left). As in previous cases, we made a fit following the C IV λ1549 fit.
2. *J02287+0002*. This object has a very complex spectrum. On the one hand it has an FWHM(BC) ≈ 4700 km s^{-1}. Considering that the FWHM limit between Pop. A and B is increasing with luminosity, the FWHM(BC) is within the limit of Pop. A, but close to the boundary with Pop. B. The line profiles are better fit with Lorentzians. On the other hand, however, it shows features that are typical of extreme Pop. A sources: prominent Fe II λ1787, strong Al III λ1860, no C III] λ1909 VBC (Figure 4, middle right). The C III] λ1909 line is not very flat topped, but the similar intensities of C III] λ1909 and Si III] λ1892 are reminiscent of the case of J02390−0038. We assign J02287+0002 to Pop. A because it has a strong blueshifted component in C IV λ1549 atypical to Pop. B objects (Figure 4, middle center). The C IV λ1549 BAL shows a blueshift of 9100 km s^{-1} at the deepest absorption, an EW of –14 Å and an FWHM of 4600 km s^{-1}. The starting and terminal velocities of the trough range from −6600 to −15,100 km s^{-1} (considering the $z_{\rm O\,I}$ rest frame). As in the case of J01225+1339, the Si IV λ1397 + O IV] λ1402 blend profile is severely affected by two broad absorption lines on both sides (Figure 4, middle left).
The estimated rest frame of this quasar differs by ∼1300 km s^{-1} using O I λ1304 and C III] λ1909. This is the largest discrepancy in our sample. In order to evaluate the effect of the z discrepancy, we performed two fits using both rest frames. The middle panels of Figure 4 use the O I

λ1304 rest frame. In the 1900 Å blend, we found a contribution of Si III] λ1892 similar to C III] λ1909. If we use the C III] λ1909 inferred rest frame that we show in the lower panels of Figure 4, C III] λ1909 becomes stronger with a resultant decrease of Si III] λ1892. A similar effect occurs for C IV λ1549 broad and blue-shifted components.

Summing up, we are able to assign a Pop. A/B identification to all sources in our sample. The two BAL quasars appear as objects of extreme Pop. A; for J02287+0002 the assignment depends on the assumed redshift. However, the most likely estimate—based on the O I λ1304 line and is $z \approx 2.726$—implies Pop. A features. Figure 4 stands as a neat example of the importance of accurate redshift determination for quasars, as the interpretation of the source spectrum can be made different by a $\Delta z \approx 0.0097$.

6. DIAGNOSTICS OF IONIZING PHOTON FLUX

The physical conditions of photoionized gas can be described by electron density n_e, hydrogen column density N_c, metallicity (Z; normalized to solar), the shape of the ionizing continuum, and the ionization parameter U. The latter represents the dimensionless ratio of the number of ionizing photons and the electron density n_e or, equivalently, the total number density of hydrogen n_H, ionized and neutral.[6] Both U and n_H are related through the equation

$$U = \frac{\int_{\nu_0}^{+\infty} \frac{L_\nu}{h\nu} d\nu}{4\pi n_H c r^2} = \frac{Q(H)}{4\pi n_H c r^2}, \quad (1)$$

where L_ν is the specific luminosity per unit frequency, h is the Planck constant, ν_0 the Rydberg frequency, c the speed of light, and r can be interpreted as the distance between the central source of ionizing radiation and the line emitting region. $Q(H)$ is the number of H-ionizing photons. Note that $n_H U$ is, apart from the constant c, the ionizing photon flux

$$c\, n_H U = \Phi(H) = \frac{Q(H)}{4\pi r^2}. \quad (2)$$

If we know *the product of* n_H and U, we can estimate the radius r of the BLR from Equation (1):

$$r_{BLR,\Phi} = \sqrt{\frac{Q(H)}{4\pi c (n_H U)}}. \quad (3)$$

$r_{BLR,\Phi}$ is the "photoionization" r_{BLR} as defined in Paper I. The dependence of U on r_{BLR} was used by Padovani & Rafanelli (1988) to derive central black hole masses assuming a plausible average value of the product $n_H U$. The typical value of n_e was derived at that time from a semiforbidden line C III] λ1909 which implied that the density could not be much higher than $n_e \approx 10^{9.5}$ cm^{-3} (Osterbrock & Ferland 2006). Padovani & Rafanelli (1988) derived an average value $\langle U \cdot n_e \rangle \approx 10^{9.8}$ from several sources where r_{BLR} had been determined from reverberation mapping, and for which the number of ionizing photons could be measured from multiwavelength observations. The average value was then used to compute black hole masses for a much larger sample of Seyfert 1 galaxies and low-z quasars (Padovani & Rafanelli 1988; Padovani et al. 1990). Wandel et al. (1999) compared the results of the photoionization method with the ones obtained through reverberation mapping, found a very good correlation for the masses computed with the two methods, and concluded that "both methods measure the mass of the central black hole." A similar method based on the Hβ luminosity was proposed by Dibai (1984), who retrieved the ionizing luminosity from the luminosity of Hβ. Bochkarev & Gaskell (2009) verified that Dibai mass estimates agree with reverberation-mapping mass estimates.

In Paper II we showed that the ionizing photon flux estimated from UV lines is also in close agreement with reverberation mapping BLR distance from continuum source. Photoionization methods can at least provide an alternative method to deduce r_{BLR} with an accuracy comparable to reverberation mapping. The approach of this paper follows from the results of Paper II, in which intermediate ionization lines and HIL are used as a diagnostic of the ionizing photon flux. There are three main issues that are of relevance for a general population of quasars: the actual physical conditions within the BLR, and specifically the contribution of relatively low density gas ($n_H \sim 10^{10}$ cm^{-3}). A third special issue is the estimate of the quasar metallicity, because previous studies agree on super solar metallicity for high z quasars (e.g., Hamann & Ferland 1993; Ferland et al. 1996; Nagao et al. 2006; Simon & Hamann 2010).

6.1. Physical Conditions in the Emitting Regions

The method used to estimate the physical conditions of the emitting region is described in Paper I. Here we summarize the basic aspects, as well as the complications arising from dealing with sources that are different from extreme sources Pop. A. To this aim, we apply and further develop the empirical technique that has been discussed in Paper II.

We base our interpretation of line ratios on a multidimensional grid of CLOUDY (Ferland et al. 1998, 2013) simulations (see also Korista et al. 1997) to derive U and n_H from our spectral measurements. Simulations span the density range $7.00 \leqslant \log n_H \leqslant 14.00$, and $-4.50 \leqslant \log U \leqslant 00.00$, in intervals of 0.25. Each simulation was computed for a fixed ionization parameter and density, assuming plane parallel geometry. The two-dimensional grid of simulations was repeated twice, assuming $N_c = 10^{23}$ and 10^{24} cm^{-2}. Several cases were also computed for $N_c = 10^{25}$ cm^{-2}. Metallicity was assumed to be either solar or five times solar. Two alternative input continua were used: (1) the standard AGN continuum of CLOUDY that is equivalent to the continuum described by Mathews & Ferland (1987), and (2) the low-z quasar continuum of Laor et al. (1997b). Computed line ratios are almost identical for fixed (U, n_H). For this paper we use the (U, n_H) maps computed for the Laor et al. (1997b) continuum (Figure 5 of Paper I). It is the ionizing luminosity that differs by more than a factor of two for a fixed specific continuum luminosity (as considered in Section 8), since the same U is reached at smaller distance for the continuum with fewer ionizing photons. This is taken into account when estimating r_{BLR} (Section 8).

Feldman et al. (1992) give a critical density value for Si III] λ1892 $n_e \sim 2 \times 10^{11}$ cm^{-3}. Al III λ1860 is a permitted transition with large transition probability ($A \sim 5 \times 10^8$ s^{-1}) and has a very high and ill-defined critical density (i.e., its equivalent width goes to zero toward thermodynamic equilibrium, which occurs at very high density when all emergent line emission is zeroed by equilibrium between collisional excitation and de-excitation). Our two-dimensional array of CLOUDY simulations shows that the ratio Al III λ1860/Si III] λ1892 is well suited to

[6] In a fully ionized medium $n_e \approx 1.2\, n_H$. We prefer to adopt the definition based on n_H because it is the one employed in the CLOUDY computations.

sample the density range 10^{10}–$10^{12.5}$ cm^{-3}. Within this range the Si III] λ1892 intensity decreases smoothly by a factor of 10; above the upper limit in density, the predicted intensity of Si III] λ1892 decreases (Paper I). The ratio Al III λ1860/Si III] λ1892 alone is, generally speaking, insufficient to constrain $n_{\rm H}$. A second diagnostic ratio is needed to constrain U and to unambiguously derive $n_{\rm H}$. We consider C IV λ1549/Si III] λ1892 and Si IV λ1397+O IV] λ1402/Si III] λ1892 as two diagnostic ratios suitable for constraining U.

6.2. The Contribution of Lower Density Gas

The presence of significant C III] λ1909 emission complicates the analysis. As pointed out, the photoionization solution for the BC suggests very high density, and in this region no C III] λ1909 emission is expected. The ratio Al III λ1860/Si III] λ1892 diagnosis high density gas, while the C III] λ1909/Si III] λ1892 ratio covers the domain of $n_{\rm H} \sim 10^{10}$ cm^{-3}. The spatially unresolved line emission is probably a mixture of gas in a different density ionization condition, possibly following a smooth gradient. The much lower C III] λ1909 critical density implies that the C III] λ1909 line should be formed farther out than Si III] λ1892 and Al III λ1860 if all these lines are produced under similar ionization conditions.

For the BAL quasars in our sample and Al III λ1860-strong sources, most of what we ascribe to C III] λ1909 could actually be Fe III, as suggested by Hartig & Baldwin (1986). For Pop. A sources of spectral types A3 and A4, as well as for BAL quasars belonging to these A spectral types where C III] λ1909 is weak with respect to Si III] λ1892, any contribution due to lower density gas could be neglected.

Among Pop. A2 and some A3 objects it is not so obvious that the profile of C III] λ1909 and Si III] λ1892 is the same. It could be that the C III] λ1909 profile is narrower than that of Si III] λ1892 and Al III λ1860 (as found for SDSS J12014+0116, see Paper I), justifying the idea of C III] λ1909 emission from a disjoint region or perhaps from the lower-density tail of comet-shaped clouds (Maiolino et al. 2010). Reverberation mapping studies of the 1900 Å blend are scant, but indicate that time delays in C III] λ1909 are a factor of two to three larger than in C IV λ1549 (Onken & Peterson 2002; Metzroth et al. 2006).

Whenever strong C III] λ1909 is observed, as in the case of spectral type A1 and A2 and even more of Pop. B, we could reverse the question: how much does any C III] λ1909 emitting gas contribute to the lines used for diagnostic ratios? Negligible contribution is expected for Al III λ1860. However, this is not true for C IV λ1549 and Si III] λ1892. A realistic estimate of the low density contribution to C IV λ1549 and Si III] λ1892 flux will depend on the assumptions concerning the ionization and density gradient, and will therefore be model dependent.

In Paper II we showed that diagnostic ratios involving C III] λ1909 are not representative of Hβ emitting gas that is responding to continuum variations. Diagnostic ratios with C III] λ1909 will be avoided. Here we will follow the same approach applying an empirical correction dependent on the ratio Al III λ1860/C III] λ1909. Generally speaking, the $n_{\rm H}U$ value derived from the ratios Al III λ1860/Si III] λ1892 and Si III] λ1892/C IV λ1549 is associated to a single point in the parameter plane ($n_{\rm H}$, U). This corresponds to a well defined solution that is biased toward high density (and therefore low $r_{\rm BLR}$). As a consequence, the BLR physical conditions cannot be described by a single value of density and ionization parameter. Even the time lag from reverberation should be interpreted with some care, because it is a single number that is a rather abstract representation of the BLR distance from the central continuum source and may not have a well-defined structural counterpart (Devereux 2013). Nonetheless, a correction based on the Al III λ1860/C III] λ1909 ratio can lower the product $n_{\rm H}U$ increasing the derived $r_{\rm BLR}$ and minimize the bias in the photoionization estimates with respect to reverberation lag (i.e., the product of the speed of light multiplied by the time lag, $c\tau$), as shown in Paper II. We apply the following correction to the derived $r_{\rm BLR}$:

$$\log r_{\rm BLR,\phi} - \log c\tau \approx 0.69 \log W(\text{Al III } \lambda 1860)/\text{W(C III] } \times \lambda 1909) + 0.49. \quad (4)$$

This is the same correlation found by Paper II updated including an improved $c\tau$ value (Negrete et al. 2014).

6.3. Metallicity

In high z quasars, the strength of N V λ1240 relative to C IV λ1549 and He II λ1640 suggests supersolar chemical abundances (Hamann & Ferland 1993, 1999). Chemical abundances may be well five to 10 times solar (Dhanda et al. 2007), with $Z \approx 5Z_{\odot}$ reputed typical of high z quasars (Ferland et al. 1996). The E1 sequence seems to be mainly a sequence of ionization in the sense of a steady decrease in prominence of the low-ionization BC toward Pop. B (Marziani et al. 2001, 2010). However, this is not to neglect that metal-enrichment also plays a role, especially for the most extreme Pop. A sources (i.e., those in bin A3 and higher Sulentic et al. 2001, 2013).

The lines employed in the present study come from carbon, silicon, and aluminum; all these elements can be significantly depleted from gas if dust grains are formed (e.g., Mathis 1990). However, the emitting regions where our lines are produced are thought to be too hot to contain a significant amount of dust (a definition of BLR is right, the central engine region below the dust sublimation region: e.g., Elitzur 2009). In addition, Si and Al are expected to be produced under similar circumstances in the late stage of evolution of massive stars (Clayton 1983, chap. 7). We considered three metallicity cases: solar, constant solar abundance ratio Al:Si:C with $Z = 5\,Z_{\odot}$ (5Z), and an overabundance of Si and Al with respect to carbon by a factor three, again with $Z = 5\,Z_{\odot}$ (5ZSiAl) following Paper I. This condition comes from the yields listed by Woosley & Weaver (1995) from type II supernovae, and is meant to represent extreme cases associated with a circumnuclear burst of star formation significantly affecting the BLR gas chemical composition (e.g., Sani et al. 2010; Paper I).

Two additional arrays of simulations as a function of the ionization parameter and density were computed assuming the metallicity conditions (2) and (3) listed in the previous paragraph. If solar metallicity is simply scaled by a factor (5Z), the ratio Al III λ1860/Si III] λ1892 is not strongly dependent on Z because it increases by about 40% passing from $Z = 1\,Z_{\odot}$ to $Z = 5\,Z_{\odot}$, for $\log n_{\rm H} \approx 12$ and $\log U \approx -2$. The same is true for the Si II λ1814/Si III] λ1892 and Si IV λ1397+O IV] λ1402/Si III] λ1892 ratios, and for the ratios involving C IV λ1549 in case 5Z (and it should be even more so if a metallicity increase is $1 \lesssim Z/Z_{\odot} \lesssim 5$). Therefore, we do not expect that the ratios employed are sensitive to Z; this is a major advantage of the method and will be verified a posteriori (Section 7.2). To gain some information on Z, we consider the ratio Si IV λ1397+O IV] λ1402/C IV λ1549 that has been extensively used in the investigation of metallicity for low and high-z quasars (e.g., Nagao et al. 2006) and is fairly well correlated with N V λ1240/Lyα (Shin et al. 2013). We

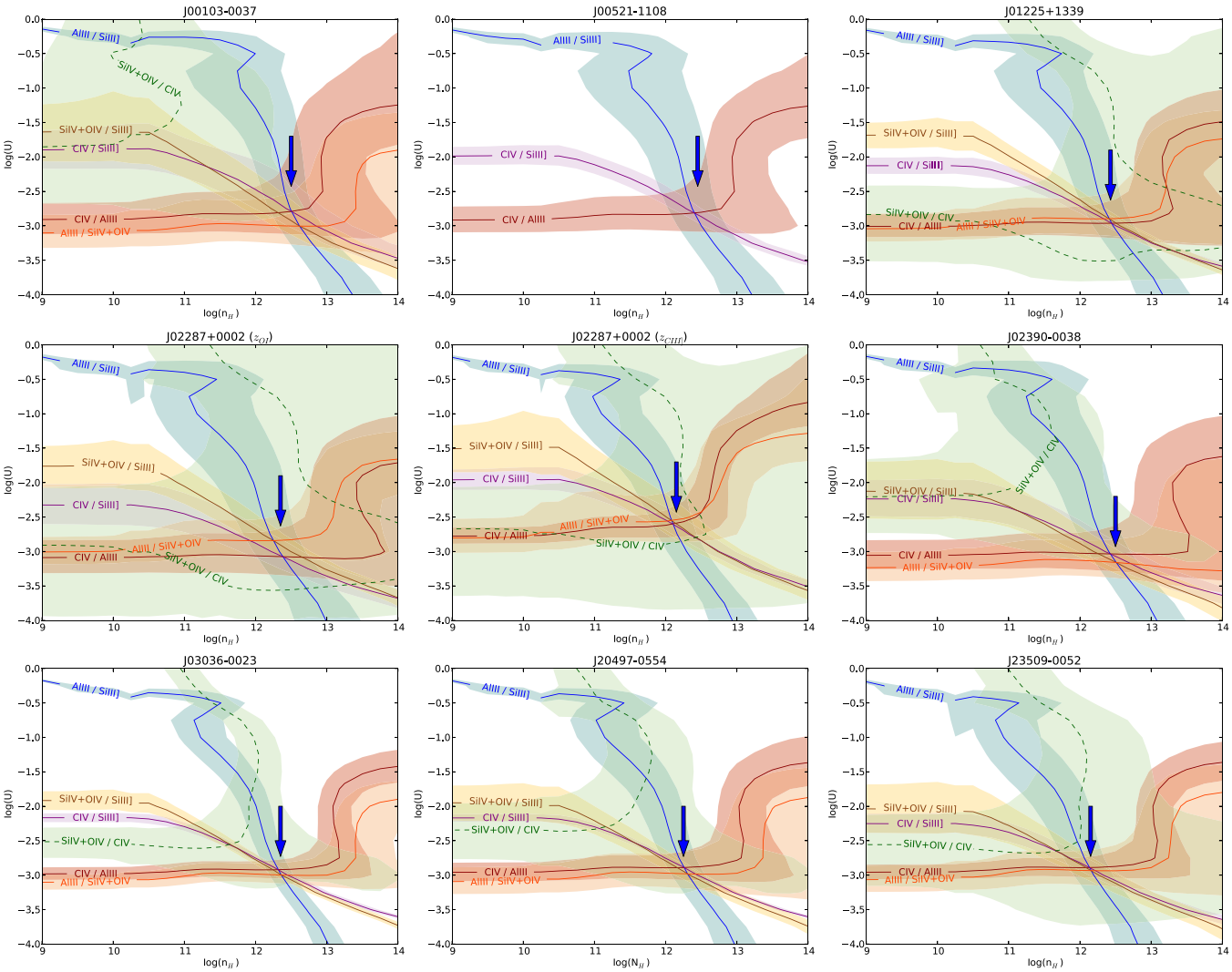

Figure 6. Contour plots for our sample. We show the two cases for the BAL quasar J02287+0002. Abscissa is electron density in cm^{-3}, ordinate is the ionization parameter, both in logarithm scale. The point where the isocontours cross (marked with an arrow) determines the values of log$n_{\rm H}$ and log$U$. Si IV λ1397+O IV] λ1402/C IV λ1549 is in dashed line because we do not use it to constrain $n_{\rm H}U$, but to determine the metallicity (see Section 6.3). The shaded areas are the error bands at 2σ confidence.

(A color version of this figure is available in the online journal.)

avoid considering the ratio involving N v λ1240 because the deblending is extremely difficult without a very careful model of Lyα that is customarily heavily affected by narrow absorptions; and using Lyα will restrict the redshift range for which this method can be employed with our resorting to far UV space-based observations, from a minimum $z \approx 1.4$ to $z \approx 2.0$. In addition, the goal of the present method is to estimate $r_{\rm BLR}$, not Z; we only try to analyze how Z can affect $r_{\rm BLR}$.

7. RESULTS ON THE $z \approx 3$ QUASARS

7.1. The Ionizing Photon Flux

To estimate log $n_{\rm H}U$ we use the CLOUDY contour plots of the ratios Al III λ1860/Si III] λ1892, C IV λ1549/Si III] λ1892, Si IV λ1397+O IV] λ1402/Si III] λ1892, C IV λ1549/Al III λ1860, Al III λ1860/Si IV λ1397+O IV] λ1402 and Si IV λ1397+O IV] λ1402/C IV λ1549 shown in Figure 5 of Paper I.[7] The data points of our objects are in regions where the ratios are well defined. The ratio Si IV λ1397+O IV] λ1402/C IV λ1549 is used only to give a hint of the metallicity (see Section 7.2). The ratios C IV λ1549/Si III] λ1892, Si IV λ1397+O IV] λ1402/Si III] λ1892, C IV λ1549/Al III λ1860 and Al III λ1860/Si IV λ1397+O IV] λ1402 are mainly sensitive to the ionization parameter U, while Al III λ1860/Si III] λ1892 and C III] λ1909/Si III] λ1892 are mainly sensitive to density (the latter is not considered in the following as discussed in Section 6.2).

The diagnostic ratios were computed from the intensity of the BC of Si III] λ1892, Al III λ1860, Si IV λ1397 and C IV λ1549 reported in Table 2. We display on a graph a line representing the behavior of each ratio under the assumption of solar metallicity; the ideal point where the lines representing different diagnostic ratios cross, determines the values of log$n_{\rm H}U$. Figure 6 shows the contour plots where we can see that the diagnostic ratios (except Si IV λ1397+O IV] λ1402/C IV λ1549) converge to rather well defined values. The crossing point is very precise for the objects J00521−1108, J01225+1339, J02287+0002 (using $z_{\rm C\,III]}$), J02390−0038, J03036−0023, J20497−0554, and J23509−0052; for the remaining objects J00103−0037

[7] Note that there are regions where the ratio values are actually undefined: close to the high U limit (log $U \gtrsim -0.3$), ratio Al III λ1860/Si III] λ1892 (with $n_{\rm H} \lesssim 10^9$ cm^{-3}) should not be considered.

Table 5
Hydrogen Density and Ionization Parameter

Object	Log $n_{\rm H}$			Log U			Log $n_{\rm H}U$		
	$1Z_\odot$	$5Z_\odot$	$5Z_\odot$ SiAl	$1Z_\odot$	$5Z_\odot$	$5Z_\odot$ SiAl	$1Z_\odot$	$5Z_\odot$	$5Z_\odot$ SiAl
J00103−0037	**12.50 ± 0.17**	...	...	**−2.79 ± 0.19**	...	...	**9.71 ± 0.22**	...	...
J00521−1108	**12.37 ± 0.26**	...	...	**−2.74 ± 0.15**	...	...	**9.63 ± 0.27**	...	...
J01225+1339	12.43 ± 0.22	**11.99 ± 0.31**	11.58 ± 0.28	−2.93 ± 0.09	**−2.44 ± 0.39**	−2.04 ± 0.11	9.51 ± 0.21	**9.55 ± 0.43**	9.54 ± 0.27
J02287+0002[(1)]	12.32 ± 0.15	11.88 ± 0.23	**11.33 ± 0.38**	−2.96 ± 0.24	−2.55 ± 0.40	**−2.13 ± 0.22**	9.36 ± 0.24	9.33 ± 0.40	**9.21 ± 0.38**
J02287+0002[(2)]	**12.10 ± 0.32**	...	...	**−2.57 ± 0.28**	-...	...	**9.53 ± 0.36**	...	...
J02390−0038	**12.47 ± 0.12**	...	...	**−3.10 ± 0.05**	...	...	**9.38 ± 0.11**	...	...
J03036−0023	**12.34 ± 0.14**	...	...	**−2.96 ± 0.06**	...	...	**9.39 ± 0.14**	...	...
J20497−0554	**12.28 ± 0.25**	...	...	**−2.93 ± 0.12**	...	...	**9.35 ± 0.25**	...	...
J23509−0052	**12.15 ± 0.24**	...	...	**−2.91 ± 0.09**	...	...	**9.24 ± 0.24**	...	...

Notes. (1) Considering $z_{\rm O\,I}$. (2) Considering $z_{\rm C\,III]}$. We show in bold numbers the ones that we consider the best.

and J02287+0002 (using $z_{\rm O\,I}$), the crossing point is slightly different.

Table 5 summarizes the $\log n_{\rm H}$ and $\log U$ values including their uncertainty. Since U and $n_{\rm H}$ are not independent quantities (their correlation coefficient is found to be 0.55), we adopt the appropriate formula for the errors on the product $n_{\rm H}U$ (following Bevington 1969). As discussed in Paper II, $n_{\rm H}$ and U cannot be separately estimated unless a source is of extreme Pop. A.

7.2. Effects of Metallicity

The crossing point of the ratios Si IV λ1397+O IV] λ1402/Si III] λ1892 and Si II λ1814/Si III] λ1892 is in principle independent on metallicity. Therefore, any significant disagreement between this crossing point and the ratios based on C IV λ1549 may indicate a chemical composition different from the assumed solar one (Section 6.3). We note also that the C IV λ1549/Si III] λ1892 and C IV λ1549/Al III λ1860 usually give results that are in perfect agreement in the plane ($n_{\rm H}$, U). These findings support our assumption that, if metallicity variations are present, the relative abundance of Al to Si remains constant.

We attempted to isolate a C IV λ1549 and a Si IV λ1397 component that corresponds to the Al III λ1860 and Si III] λ1892 lines. A large part of the emission in these lines is due to a BLUE component that is emitted in physical and dynamical conditions different from the ones of the BC emitting gas. C IV λ1549 shows a large blueshift and is much broader than Hβ, Si III] λ1892 and Al III λ1860 (Figure 2 of Marziani et al. 2010). In spite of this consideration, we measured the intensity of the full profile. In the case of the 1400 Å blend, we also considered the full intensity, regardless of the line components' decomposition. The 1400 Å feature is too complex of a blend for the Si IV λ1397 and O IV] λ1402 contribution to be reliably singled out for the wide majority of sources that are not extreme Pop. A (Paper I). Even if the two components emitted under different physical and/or dynamical conditions are responsible for the 1400 Å blend, the chemical composition of both components is expected to be the same (and in this case the full C IV λ1549 intensity was used for normalization). In addition, the 1400 Å full blend intensity normalized by full C IV λ1549 intensity has been used as a metallicity indicator in recent works (e.g., Nagao et al. 2006; Shin et al. 2013).

Generally speaking, appreciable discrepancies in the crossing point of the 1400 Å/C IV λ1549 ratio may signal a non-solar metallicity yielding a higher and lower 1400 Å/C IV λ1549 ratio in the case of super solar and sub-solar metallicity, respectively, for a given ionization and density solution. However, the 1400/C IV λ1549 ratio does not provide a good constraint of metallicity because the uncertainty bands in the ($n_{\rm H}$, U) plane are very large. In the case of the BAL quasars J01225+1339, and J02287+0002 if z O I λ1304 is assumed, this ratio gives some indication of super solar metallicity. For this reason, we calculated contour plots with higher metallicity values. These new plots are shown for J01225+1339 and J02287+0002 in Figure 7 in the case of $5\,Z_\odot$ and $5\,Z_\odot$SiAl metallicity. The agreement in the intersection points for J01225+1339, remains well defined in the case of $Z = 5\,Z_\odot$. For J02287+0002 the agreement in the intersection point becomes better for $Z = 5\,Z_\odot$ SiAl. The $Z = 5\,Z_\odot$SiAl case yields higher U and smaller $n_{\rm H}$ if emission line ratios involving C IV λ1549 are considered. This reflects the increase in the abundance of Si and Al, with respect to C, and the fact the Si II λ1814, Si III] λ1892, and Al III λ1860 lines are emitted at lower ionization than C IV λ1549.

In all other cases the metallicity is not well constrained, and could be well within one and five times solar. In order to be sure, however, we repeated the $n_{\rm H}U$ derivation for all sources in the $5\,Z_\odot$ case. There is no systematic difference and the dispersion is also less than the estimated $n_{\rm H}U$ uncertainties: $< n_{\rm H}U(1\,Z_\odot) - n_{\rm H}U(5\,Z_\odot) > \approx -0.02$, with rms ≈ 0.09. If a solar metallicity had been assumed for J02287+0002, $n_{\rm H}U(1\,Z_\odot) - n_{\rm H}U(5\,Z_\odot{\rm SiAl}) \approx 0.16$. Significant changes are expected only in the cases that there is a selective enhancement of some elements over others involved in the computation of the diagnostic intensity ratios. The average effect would be $n_{\rm H}U(1\,Z_\odot) - n_{\rm H}U(5\,Z_\odot{\rm SiAl}) \approx 0.11$ with an rms of ≈0.2. We do not report all super solar cases in Table 5 because they are not believed to be correct, save for J02287+0002 and J01225+1339. The numbers in bold identify the preferred Z ($n_{\rm H}$, U) solutions.

We conclude that scaling the metallicity up to $Z = 5\,Z_\odot$ from $Z = 1\,Z_\odot$ yields an effect that is well below the uncertainty associated with the method, and particularly small if the ratios Al III λ1860/Si III] λ1892, Si IV λ1397+O IV] λ1402/Si III] λ1892 and C IV λ1549/Al III λ1860 are considered to compute $n_{\rm H}$ and U. It is significant if strong enrichment of Al and Si over C occurs, so that the efforts should be focused on the identification of such cases. These cases are, however, believed to be relatively rare (≈10% at low z), and are easily identified because they generally satisfy the condition Al III λ1860 $\gtrsim$ 0.5 Si III] λ1892, and Si III] λ1892 $\gtrsim$ C III] λ1909 (Marziani & Sulentic 2014).

8. PHOTOIONIZATION COMPUTATIONS OF BROAD LINE REGION DISTANCE AND BLACK HOLE MASS

The distance of the BLR $r_{\rm BLR}$ and the black hole mass ($M_{\rm BH}$) are key parameters that let us understand the dynamics of the

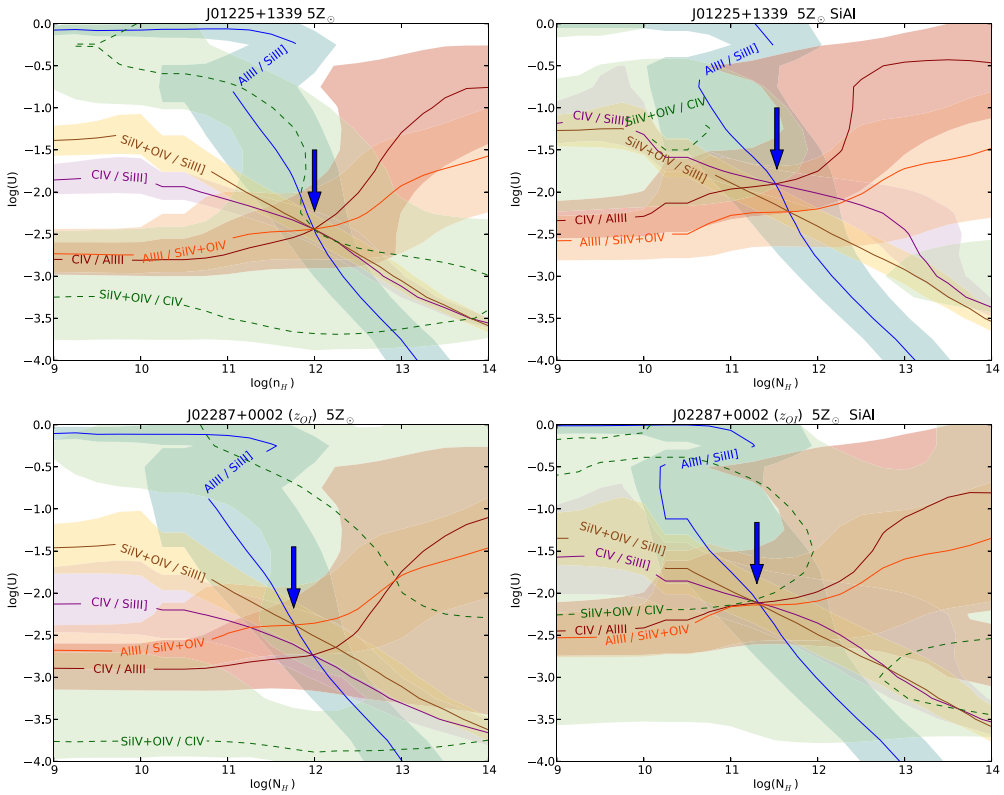

Figure 7. Left: contour plots from the array of simulations computed for $Z = 5\ Z_{\odot}$. Right: same as left panels, considering the case of overabundance of Si and Al. Upper panels are for J01225+1339. Lower panels are for J02287+0002 considering $z_{\rm O\,I}$. Coordinates and symbols are as for Figure 6. The intersection point improves in certain cases, but in others it is the same.

(A color version of this figure is available in the online journal.)

gas in the emitting region and the quasar behavior and evolution. In this work we will use a method based on the determination of $n_{\rm H}U$ to compute $r_{\rm BLR,\Phi}$. Equation (3) can be rewritten as

$$r_{\rm BLR,\Phi} = \frac{1}{h^{1/2}c}(n_{\rm H}U)^{-1/2}\left(\int_0^{\lambda_{Ly}} f_\lambda \lambda d\lambda\right)^{1/2} d_c, \qquad (5)$$

where d_c is the radial comoving distance. The integral is carried out from the Lyman limit ($\lambda_{\rm Ly}$) to the shortest wavelengths on the *rest frame* specific flux f_λ. For the integral we will use two spectral energy distributions (SEDs): one described by Mathews & Ferland (1987) and one by Laor et al. (1997b).

Expressing $r_{\rm BLR,\Phi}$ in units of light-days, and scaling the variables to convenient units, Equation (5) becomes

$$r_{\rm BLR,\Phi} \approx 93\left[\frac{f_{\lambda_0,-15}\tilde{Q}_{\rm H,0.01}}{(n_{\rm H}U)_{10}}\right]^{\frac{1}{2}} \zeta(z, 0.3, 0.7)\ \text{lt-day}, \qquad (6)$$

where $f_{\lambda_0,-15}$ is the specific rest frame flux (measured on the spectra at $\lambda_0 = 1700$ Å) in units of 10^{-15} erg s^{-1} cm^{-2} Å^{-1}. The product $n_{\rm H}U$ is normalized to 10^{10} cm^{-3}. $\zeta(z, 0.3, 0.7)$ is an interpolation function of d_c as a function of redshift. $\tilde{Q}_{H,0.01} = \int_0^{\lambda_{\rm Ly}} \tilde{s}_\lambda \lambda d\lambda$ is normalized to 10^{-2} cm Å. We use $\tilde{s}_\lambda$ to define the SED following Mathews & Ferland (1987) and Laor et al. (1997b). $\tilde{Q}_H$ is 0.00963 cm Å in the case the continuum of Laor et al. (1997b) is considered; $\tilde{Q}_H \approx 0.02181$ cm Å for Mathews & Ferland (1987). We use their average value, because the derived U and $n_{\rm H}$ are not sensitive to the two different shapes to a first approximation.[8] The two SEDs give a small difference in the estimated number of ionizing photons.

Knowing $r_{\rm BLR,\Phi}$ we can calculate the $M_{\rm BH,\Phi}$ assuming virial motions of the gas

$$M_{\rm BH,\Phi} = f\frac{\Delta v^2 r_{\rm BLR,\Phi}}{G} \qquad (7)$$

or,

$$M_{\rm BH,\Phi} = \frac{3}{4G} f_{0.75}(\text{FWHM})^2 r_{\rm BLR,\Phi} \qquad (8)$$

with the geometry term $f_{0.75} \approx 1.0$ (Graham et al. 2011, see also Onken et al. 2004; Woo et al. 2010). Collin et al. (2006) suggest that f is significantly different for Pop. A and B sources; here we do not consider their important result for the sake of comparison with previous work (Section 9.2).

Table 6 reports the values of the $r_{\rm BLR,\Phi}$ and the $M_{\rm BH,\Phi}$ of our eight objects and the extreme objects in the last two rows. Column 1 identifies the quasar name; Column 2 gives the quasar comoving distance in mega parsecs (Mpc); Columns 3 and 4 are the continuum specific flux value at 1350 Å and 1700 Å respectively, Column 5 reports the FWHM in km s^{-1} for the BCs, Column 6 is the population designation. Columns 7 and 8 report the logarithm of the $r_{\rm BLR}$ in cm obtained from: (1) the values selected from Table 5 ($r_{\rm BLR,\Phi}$); and (2) corrected by low density emission using Equation (4). Columns 9 and 10 list the determinations of $M_{\rm BH}$ in solar masses in the same order as for $r_{\rm BLR}$. Finally Columns 11 and 12 are $M_{\rm BH}$ computed following

[8] Since the Laor et al. (1997b) continuum produces a fewer ionizing photons, the same value of U is obtained at a smaller distance.

Table 6
The Size of the Broad Line Region and the Black Hole Masses

Object	d_C	f(1700 Å)[a]	f(1350 Å)[a]	FWHM$_{BC}$	Pop.	log(r_{BLR}) (cm)		log(M_{BH}) ($M_\odot$)[b]			
	(Mpc)	$X10^{-15}$	$X10^{-15}$	(km s^{-1})		ϕ[e]	Low Dens[e]	ϕ[e]	Low Dens[e]	VP06[b]	S12[c]
(1)	(2)	(3)	(4)	(5)	(6)	(7)	(8)	(9)	(10)	(11)	(12)
J00103−0037	6510	4.8 ± 1.0	6.8 ± 1.4	4500 ± 1200	B	18.10 ± 0.12	17.90 ± 0.14	9.29 ± 0.26	9.08 ± 0.27	9.11	9.17
J00521−1108	6586	6.1 ± 1.5	8.8 ± 2.1	5300 ± 1600	B	18.20 ± 0.15	17.93 ± 0.25	9.53 ± 0.30	9.25 ± 0.37	9.32	9.24
J01225+1339	6415	8.1 ± 1.6	10.9 ± 2.2	4400 ± 1000	A[d]	18.29 ± 0.15	18.08 ± 0.25	9.45 ± 0.25	9.24 ± 0.32	9.19	9.25
J02287+0002(1)	6091	7.4 ± 2.7	8.4 ± 3.0	3900 ± 1200	A	18.42 ± 0.21	18.22 ± 0.21	9.48 ± 0.34	9.28 ± 0.34	9.00	9.17
J02287+0002(2)	6091	7.4 ± 2.7	8.4 ± 3.0	4100 ± 1200	A[d]	18.26 ± 0.20	18.19 ± 0.21	9.36 ± 0.32	9.29 ± 0.33	9.05	9.17
J02390−0038	6448	6.9 ± 2.1	9.9 ± 3.0	4600 ± 1000	A[d]	18.34 ± 0.16	18.10 ± 0.16	9.55 ± 0.25	9.30 ± 0.25	9.21	9.24
J03036−0023	6582	20.5 ± 5.7	30.0 ± 8.4	3700 ± 600	A	18.58 ± 0.10	18.39 ± 0.15	9.60 ± 0.17	9.40 ± 0.21	9.29	9.45
J20497−0554	6552	6.6 ± 1.3	9.5 ± 1.9	3800 ± 600	A	18.35 ± 0.13	18.17 ± 0.22	9.39 ± 0.19	9.21 ± 0.26	9.04	9.22
J23509−0052	6398	4.8 ± 1.0	6.1 ± 1.2	3600 ± 800	A	18.33 ± 0.19	18.22 ± 0.23	9.32 ± 0.27	9.21 ± 0.30	8.88	9.11

Notes.
[a] Units of the flux at 1350 and 1700 Å are in erg s^{-1} cm^{-2} Å^{-1}. We show the comparison between our computations and those using:
[b] The Vestergaard & Peterson (2006) method.
[c] The Shen & Liu (2012) work. They report an uncertainty of 0.66 and 0.54 dex at 2σ confidence, respectively.
[d] FWHM > 4000 km s^{-1}, but the sources have other spectral characteristics of Pop. A objects and belong to Pop. A if the luminosity-dependent definition of Marziani et al. (2009) is applied (see Section 5).
[e] The listed values computed assuming an average SED of Laor et al. (1997b) and Mathews & Ferland (1987) with a scatter ±0.17 dex. We used the bold numbers of Table 5 to compute $r_{BLR,\Phi}$. (1) Considering $z_{O\,I}$. (2) Considering $z_{C\,III]}$.

Vestergaard & Peterson (2006, their Equation (11)) and Shen & Liu (2012), respectively. We will explain in Section 9 how these quantities are computed.

9. DISCUSSION

9.1. Previous Work

There have been several studies aimed at computing r_{BLR} and M_{BH}. A direct measure of r_{BLR} through reverberation mapping requires an enormous amount of observational effort and has only been applied to a relatively small number of quasars: slightly less than 60 objects with $z \lesssim 0.4$ (Kaspi et al. 2000, 2005; Peterson et al. 2004; Bentz et al. 2010, 2013). A second way to measure r_{BLR} uses a less direct method. Kaspi et al. (2000, 2005) and Bentz et al. (2009) used reverberation mapping results to find, in an empirical way, a relation between r_{BLR} and the optical continuum luminosity at 5100 Å,

$$r_{BLR} \propto L^{\alpha} \quad (9)$$

with $\alpha \approx 0.52$. Vestergaard & Peterson (2006) obtained a similar result for the optical continuum luminosity with an $\alpha \approx 0.50$ and for the UV continuum at 1350 Å, $\alpha \approx 0.53$. These relations have been used to compute the r_{BLR} not only for nearby objects, but also for high redshift, high luminosity objects. There are other works that use single epoch spectra and the continuum at 3000 Å, obtaining an $\alpha \approx 0.47$ (McLure & Jarvis 2002).

We can rewrite Equation (7) as

$$M_{BH} \propto f \frac{\mathrm{FWHM}^2 L^{\alpha}}{G}. \quad (10)$$

H β is a low ionization strong line whose FWHM has been widely used to determine the M_{BH} for objects mainly up to $z \lesssim 0.9$; above this limit IR spectrometers and large telescopes are needed to cover the redshifted line. For distant objects ($z \sim 2$), an alternative is to use C IV λ1549, an HIL emitted in the UV. However, this line should be used with caution because the line is often blueshifted. This means that at least part of this line is likely emitted in an outflow (Netzer et al. 2007; Richards et al. 2011; Marziani & Sulentic 2012). Thus the estimation of M_{BH} using FWHM (C IV λ1549) tend to be systematically higher than those using FWHM(Hβ) for objects of Pop. A (Sulentic et al. 2007).

9.2. Comparison with Previous Work

We compare $r_{BLR,\Phi}$ obtained using our photoionization method with the ones estimated through the r_{BLR}–L correlation in the upper panel of Figure 8. Our $r_{BLR,\Phi}$ agree well with the Bentz et al. (2013) relation: the average $r_{BLR,\Phi}$–$r_{BLR}(L)$ is $\approx 0.14 \pm 0.10$ and -0.16 ± 0.13 without and with low-density correction, respectively.

Vestergaard & Peterson (2006, hereafter VP06) used the relation $r_{BLR} \propto L^{0.53}$ to obtain the following formula that relates M_{BH} to the FWHM (C IV λ1549) and the continuum luminosity at 1350 Å:

$$\log M_{BH}(\mathrm{C\,IV}) = 0.66 + 0.53 \log \left[\frac{\lambda L_\lambda(1350\,\text{Å})}{10^{44}\ \mathrm{ergs\ s^{-1}}}\right] + 2 \log \left[\frac{\mathrm{FWHM\ (C\,IV)}}{\mathrm{km\ s^{-1}}}\right] - s_f. \quad (11)$$

More recently, Shen & Liu (2012, S12) updated the M_{BH}—luminosity relation:

$$\log M_{BH}(\mathrm{C\,IV}) = 7.295 + 0.471 \log \left[\frac{\lambda L_\lambda(1350\,\text{Å})}{10^{44}\ \mathrm{ergs\ s^{-1}}}\right] + 0.242 \log \left[\frac{\mathrm{FWHM(C\,IV)}}{\mathrm{km\ s^{-1}}}\right] - s_f. \quad (12)$$

The scale factor $s_f \approx -0.27$ sets the masses to the f value obtained by Graham et al. (2011). In Column 9–12 of Table 6 we show our $M_{BH,\Phi}$ results with those using Equations (11) and (12). We do not apply corrections for radiation-pressure effects that are likely relevant, especially for objects radiating at large Eddington ratio (Netzer 2009; Netzer & Marziani 2010).

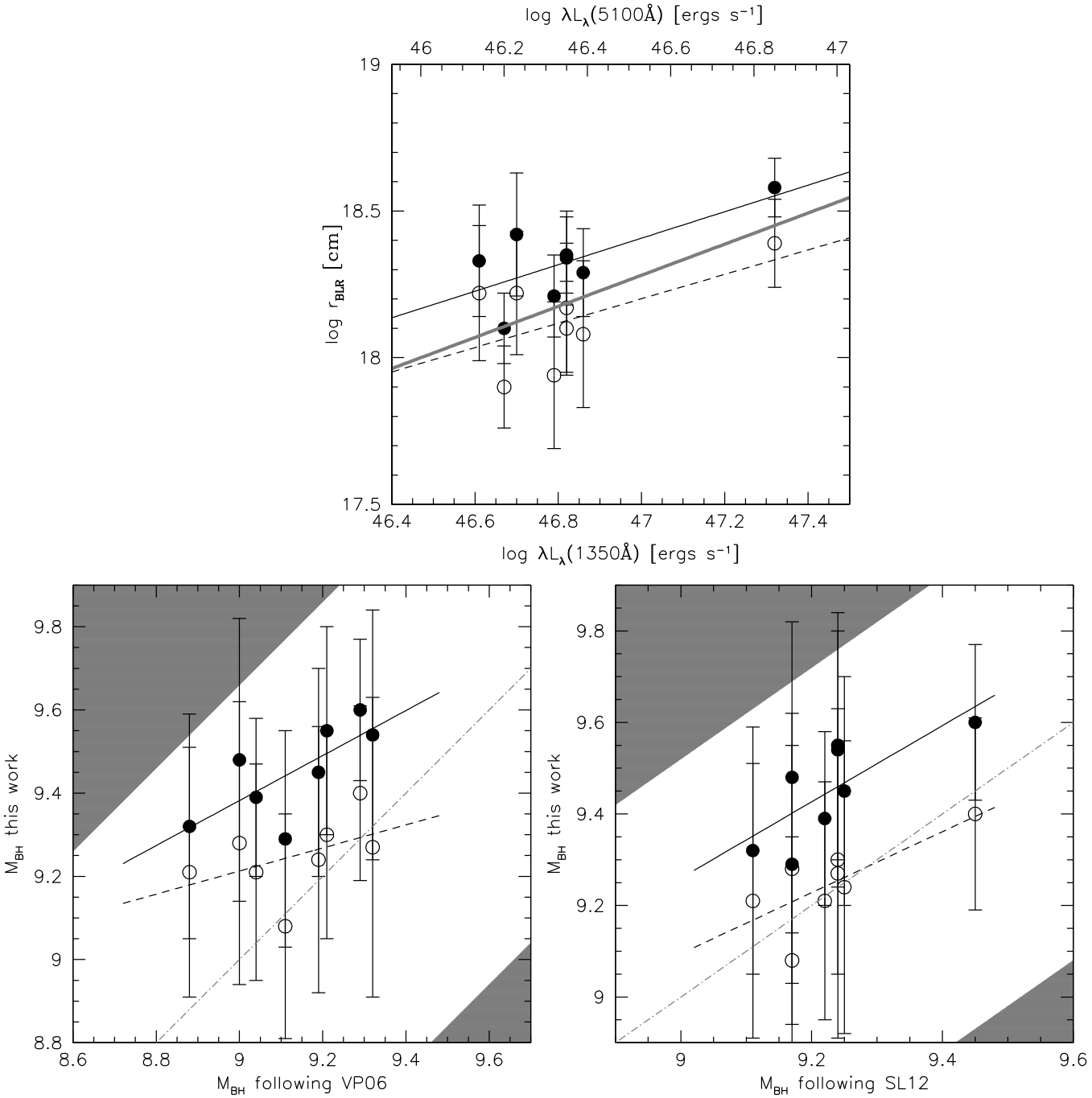

Figure 8. Upper panel: $r_{\rm BLR}$ estimates following the photoionization method with (open circles) and without (filled circles) correction for BLR low density/stratification, as a function of λL_λ measured at 1350 Å. The thick gray line is the $r_{\rm BLR}$–λL_λ 5100 Å correlation as derived from Bentz et al. (2013). The continuous and dashed lines are unweighted least square fits to uncorrected and corrected data, respectively. $\log[\lambda L_\lambda(1350)/\lambda L_\lambda(5100)] \approx 0.47$, in accordance with typical SEDs of quasars (Elvis et al. 1994; Richards et al. 2006). Middle panel: $M_{\rm BH}$ comparison for the high-z sample. The shaded bands limit the 2σ confidence level spread expected on the basis of the Vestergaard & Peterson (2006) relation. The gray dot–dashed line is the equality line. Filled symbols refer to uncorrected intensity ratios; open symbols are for intensity ratios corrected because of low-density emission. Bottom panel: same as middle panel, with $M_{\rm BH}$ computed from the Shen & Liu (2012) relation.

The difference between this computation and the one reported in Sulentic et al. (2007) is that in the latter work the BLUE component was not separated from the BC of C IV λ1549 just to show how larger values of FWHM (C IV λ1549) yielded $M_{\rm BH}$ much larger than the ones derived from FWHM(Hβ) in Pop. A objects.

We compare the masses obtained using our photoionization method with those of VP06 and S12 in Figure 8, middle and lower panel. We use the FWHM of the BC reported in Column 5 of Table 6 as an estimator of the virial line broadening. The photoionization masses before correction agree with the prediction of the luminosity correlation with a systematic offset of 0.32 ± 0.10 with VP06 and 0.22 ± 0.08 with SL12. The $M_{\rm BH}$ values obtained after correction for low density gas are systematically lower. This happens because the correction lowers the $r_{\rm BLR}$ and hence the $M_{\rm BH}$. The agreement after correction is very good, with $\langle \log M_{\rm BH,\Phi} - \log M_{\rm BH}({\rm VP06}) \rangle \approx 0.12 \pm 0.14$ and $\langle \log M_{\rm BH,\Phi} - \log M_{\rm BH}({\rm SL12}) \rangle \approx 0.02 \pm 0.07$. No significant differences occur if the z C III] λ1909 solution is used for J02287+0002.

Figure 8 should be looked at with two cautions. First, the correlation is dominated by the luminosity dependence of $r_{\rm BLR}$, used to compute $M_{\rm BH}$ in both cases. Second, the spread of $M_{\rm BH}$ values is small, less than one order of magnitude (and most objects have indistinguishable masses within the errors). However, our estimated error bars are smaller compared to the spread expected on the basis of the $r_{\rm BLR}$–L correlation, which is ≈0.33 for VP06 and ≈0.28 for S12 at 1σ confidence level. The two shaded bands of Figure 8 limit the region where we can expect to find data points on the basis of the $r_{\rm BLR}$–L correlation.

The present results indicate that the photoionization relations can be extended and used for high redshift objects (or at least until $z \sim 3$). In order to do this, we need:

1. spectra with S/N high enough to see the profile shape that allows decomposition of the C IV λ1549 line, especially to separate the BLUE component from the BC; and
2. to follow the methodological considerations explained in Section 4.

10. CONCLUSIONS

In this paper we presented new observations of eight high redshift quasars. The spectra were meant to provide high S/N, moderate resolution data on which the Si IV λ1397, C IV λ1549, Si III] λ1892 and Al III λ1860 emission line profiles could be accurately analyzed. Line profile fits permitted us to isolate a specific component whose intensity ratios were used to derive values of the ionizing photon flux.

These results allowed us to compute the product $n_{\rm H}U$ and hence the size of the BLR and the central black hole mass. The method described in this paper rests on the assumption of photoionization as the mechanism of gas heating, on the assumption of isotropic luminosity, and on line ratios predicted by CLOUDY simulations.

We found that the $M_{\rm BH}$ derived from the computed $r_{\rm BLR}$ and from the virial assumption are in good agreement with the ones derived from the luminosity–size relation. The photoionization method explored in this paper offers an estimate of $r_{\rm BLR}$ for each quasar, with some advantages on the $r_{\rm BLR}$ value derived from the luminosity–size correlation. The luminosity correlation suffers from large scatter and is simply extrapolated to very high luminosity without any support since there are, unfortunately, no conclusive results on reverberation of high luminosity quasars even if heroic efforts are underway (e.g., Trevese et al. 2007; Kaspi et al. 2007; Botti et al. 2010).

We repeat that our $M_{\rm BH}$ and $r_{\rm BLR}$ results are based on the product $n_{\rm H}U$ and not on values of $n_{\rm H}$ and of U taken separately. To apply the photoionization method in the most effective way, determining $n_{\rm H}U$ with the lowest uncertainty, spectral data should be of moderate resolution ($\lambda/\Delta\lambda \sim 1000$) as well as of high S/N. If the Si II λ1814 line can be measured in an accurate way, it would be possible to derive reliable estimates of $Z/Z_{\odot}$. Instead, we used Si IV λ1397+O IV] λ1402/C IV λ1549 to constrain metallicity. Only for extreme Pop. A sources, when Si III] λ1892 $\gtrsim$ C III] λ1909 , it is possible to estimate the $n_{\rm H}$, U and metallicity with very high S/N spectra.

The present exploratory analysis emphasized several sources of uncertainty. However, the parameter needed for $r_{\rm BLR}$ and $M_{\rm BH}$ computation, the product $n_{\rm H}U$, seems to be fairly stable and well-defined. Even with an error of a 0.3 in logarithm, the square root will be subject to a 0.15 uncertainty in logarithm, which is much lower than the uncertainty associated with the $r_{\rm BLR}$—luminosity correlation. The large intrinsic spread of the correlation at low luminosity and its uncertain extrapolation at very high luminosity make preferable a one-by-one determination based on the physical properties of the emitting regions.

A. Negrete and D. Dultzin acknowledge support from grants IN111610-3 and IN107313 PAPIIT, DGAPA UNAM.

REFERENCES

Appenzeller, I., Fricke, K., Fürtig, W., et al. 1998, Msngr, 94, 1
Bachev, R., Marziani, P., Sulentic, J. W., et al. 2004, ApJ, 617, 171
Baldwin, J. A., Ferland, G. J., Korista, K. T., Hamann, F., & LaCluyzé, A. 2004, ApJ, 615, 610
Baldwin, J. A., Ferland, G. J., Korista, K. T., et al. 1996, ApJ, 461, 664
Baskin, A., & Laor, A. 2005, MNRAS, 356, 1029
Becker, R. H., White, R. L., & Helfand, D. J. 1995, ApJ, 450, 559
Bentz, M. C., Peterson, B. M., Pogge, R. W., & Vestergaard, M. 2009, ApJL, 694, L166
Bentz, M. C., Walsh, J. L., Barth, A. J., et al. 2010, ApJ, 716, 993
Bentz, M. C., Denney, K. D., Grier, C. J., et al. 2013, ApJ, 767, 149
Bevington, P. R. 1969, Data Reduction and Error Analysis for the Physical Sciences (New York: McGraw-Hill)
Bochkarev, N. G., & Gaskell, C. M. 2009, AstL, 35, 287
Boroson, T. A., & Green, R. F. 1992, ApJS, 80, 109
Botti, I., Lira, P., Netzer, H., & Kaspi, S. 2010, in IAU Symp. 267, Co-evolution of Central Black Holes and Galaxies, ed. B. Peterson et al. (Cambridge: Cambridge Univ. Press), 198
Brühweiler, F., & Verner, E. 2008, ApJ, 675, 83
Clayton, D. D. 1983, Principles of Stellar Evolution and Nucleosynthesis (Chicago: Univ. Chicago Press)
Collin, S., Kawaguchi, T., Peterson, B. M., & Vestergaard, M. 2006, A&A, 456, 75
Collin-Souffrin, S., & Dumont, A. M. 1990, A&A, 229, 292
Collin-Souffrin, S., Dyson, J. E., McDowell, J. C., & Perry, J. J. 1988, MNRAS, 232, 539
Corbin, M. R. 1990, ApJ, 357, 346
Corbin, M. R. 1995, ApJ, 447, 496
Davidson, K., & Netzer, H. 1979, RvMP, 51, 715
Devereux, N. 2013, ApJ, 764, 79
Dhanda, N., Baldwin, J. A., Bentz, M. C., & Osmer, P. S. 2007, ApJ, 658, 804
Dibai, E. A. 1984, SvA, 28, 245
Dumont, A. M., & Mathez, G. 1981, A&A, 102, 1
Elitzur, M. 2009, in ASP Conf. Ser. 402, Approaching Micro-Arcsecond Resolution with VSOP-2: Astrophysics and Technologies, ed. Y. Hagiwara, E. Fomalont, M. Tsuboi, & M. Yasuhiro (San Francisco, CA: ASP), 419
Elvis, M. 2000, ApJ, 545, 63
Elvis, M., Wilkes, B. J., McDowell, J. C., et al. 1994, ApJS, 95, 1
Eracleous, M., & Halpern, J. P. 2003, ApJ, 599, 886
Espey, B. R., Carswell, R. F., Bailey, J. A., Smith, M. G., & Ward, M. J. 1989, ApJ, 342, 666
Feldman, U., Mandelbaum, P., Seely, J. F., Doschek, G. A., & Gursky, H. 1992, ApJS, 81, 387
Ferland, G. J., Baldwin, J. A., Korista, K. T., et al. 1996, ApJ, 461, 683
Ferland, G. J., Korista, K. T., Verner, D. A., et al. 1998, PASP, 110, 761
Ferland, G. J., Porter, R. L., van Hoof, P. A. M., et al. 2013, RMXAA, 49, 137
Flohic, H. M. L. G., Eracleous, M., & Bogdanović, T. 2012, ApJ, 753, 133
Francis, P. J., Hewett, P. C., Foltz, C. B., et al. 1991, ApJ, 373, 465
Gaskell, C. M. 1982, ApJ, 263, 79
Gaskell, C. M., Brandt, W. N., Dietrich, M., et al. 1999, in ASP Conf. Ser. 175, Structure and Kinematics of Quasar Broad Line Regions, ed. C. M. Gaskell et al. (San Francisco, CA: ASP)
Graham, A. W., Onken, C. A., Athanassoula, E., & Combes, F. 2011, MNRAS, 412, 2211
Hamann, F., & Ferland, G. 1993, ApJ, 418, 11
Hamann, F., & Ferland, G. 1999, ARA&A, 37, 487
Hartig, G. F., & Baldwin, J. A. 1986, ApJ, 302, 64
Hu, C., Wang, J.-M., Ho, L. C., et al. 2008, ApJL, 683, L115
Joly, M. 1987, A&A, 184, 33
Kaspi, S., Brandt, W. N., Maoz, D., et al. 2007, ApJ, 659, 997
Kaspi, S., Maoz, D., Netzer, H., et al. 2005, ApJ, 629, 61
Kaspi, S., Smith, P. S., Netzer, H., et al. 2000, ApJ, 533, 631
Korista, K., Baldwin, J., Ferland, G., & Verner, D. 1997, ApJS, 108, 401
Kriss, G. 1994, in ASP Conf. Ser. 61, Astronomical Data Analysis Software and Systems III, ed. D. R. Crabtree et al. (San Francisco, CA: ASP), 437

Laor, A., Fiore, F., Elvis, M., Wilkes, B. J., & McDowell, J. C. 1997a, ApJ, 477, 93
Laor, A., Jannuzi, B. T., Green, R. F., & Boroson, T. A. 1997b, ApJ, 489, 656
Maiolino, R., Risaliti, G., Salvati, M., et al. 2010, A&A, 517, A47
Marziani, P., & Sulentic, J. W. 2012, NewAR, 56, 49
Marziani, P., & Sulentic, J. W. 2014, MNRAS, 442, 1211
Marziani, P., Sulentic, J. W., Dultzin-Hacyan, D., Calvani, M., & Moles, M. 1996, ApJS, 104, 37
Marziani, P., Sulentic, J. W., Negrete, C. A., et al. 2010, MNRAS, 409, 1033
Marziani, P., Sulentic, J. W., Plauchu-Frayn, I., & del Olmo, A. 2013a, ApJ, 764, 150
Marziani, P., Sulentic, J. W., Plauchu-Frayn, I., & del Olmo, A. 2013b, A&A, 555, A89
Marziani, P., Sulentic, J. W., Stirpe, G. M., Zamfir, S., & Calvani, M. 2009, A&A, 495, 83
Marziani, P., Sulentic, J. W., Zamanov, R., et al. 2003a, ApJS, 145, 199
Marziani, P., Sulentic, J. W., Zwitter, T., Dultzin-Hacyan, D., & Calvani, M. 2001, ApJ, 558, 553
Marziani, P., Zamanov, R. K., Sulentic, J. W., & Calvani, M. 2003b, MNRAS, 345, 1133
Mathews, W. G., & Ferland, G. J. 1987, ApJ, 323, 456
Mathis, J. S. 1990, ARA&A, 28, 37
Matsuoka, Y., Kawara, K., & Oyabu, S. 2008, ApJ, 673, 62
McLure, R. J., & Jarvis, M. J. 2002, MNRAS, 337, 109
Metzroth, K. G., Onken, C. A., & Peterson, B. M. 2006, ApJ, 647, 901
Nagao, T., Marconi, A., & Maiolino, R. 2006, A&A, 447, 157
Negrete, C. A., Dultzin, D., Marziani, P., & Sulentic, J. W. 2012, ApJ, 757, 62
Negrete, C. A., Dultzin, D., Marziani, P., & Sulentic, J. W. 2013, ApJ, 771, 31
Negrete, C. A., Dultzin, D., Marziani, P., & Sulentic, J. W. 2014, AdSpR, 54, 1355
Netzer, H. 2009, ApJ, 695, 793
Netzer, H., Lira, P., Trakhtenbrot, B., Shemmer, O., & Cury, I. 2007, ApJ, 671, 1256
Netzer, H., & Marziani, P. 2010, ApJ, 724, 318
Onken, C. A., Ferrarese, L., Merritt, D., et al. 2004, ApJ, 615, 645
Onken, C. A., & Peterson, B. M. 2002, ApJ, 572, 746
Osterbrock, D. E., & Ferland, G. J. 2006, Astrophysics of Gaseous Nebulae and Active Galactic Nuclei (Sausalito, CA: Univ. Science Books)
Padovani, P., Burg, R., & Edelson, R. A. 1990, ApJ, 353, 438
Padovani, P., & Rafanelli, P. 1988, A&A, 205, 53
Peterson, B. M., Ferrarese, L., Gilbert, K. M., et al. 2004, ApJ, 613, 682
Peterson, B. M., & Wandel, A. 1999, ApJL, 521, L95
Punsly, B. 2010, ApJ, 713, 232
Richards, G. T. 2012, in ASP Conf. Ser. 460, AGN Winds in Charleston, ed. G. Chartas, F. Hamann, & K. M. Leighly (San Francisco, CA: ASP), 67
Richards, G. T., Kruczek, N. E., Gallagher, S. C., et al. 2011, AJ, 141, 167
Richards, G. T., Lacy, M., Storrie-Lombardi, L. J., et al. 2006, ApJS, 166, 470
Richards, G. T., Vanden Berk, D. E., Reichard, T. A., et al. 2002, AJ, 124, 1
Sani, E., Lutz, D., Risaliti, G., et al. 2010, MNRAS, 403, 1246
Shen, Y., & Liu, X. 2012, ApJ, 753, 125
Shin, J., Woo, J.-H., Nagao, T., & Kim, S. C. 2013, ApJ, 763, 58
Simon, L. E., & Hamann, F. 2010, MNRAS, 407, 1826
Sulentic, J. W., Bachev, R., Marziani, P., Negrete, C. A., & Dultzin, D. 2007, ApJ, 666, 757
Sulentic, J. W., del Olmo, A., & Marziani, P. 2013, arXiv e-prints
Sulentic, J. W., Dultzin-Hacyan, D., Marziani, P., et al. 2006a, RMxAA, 42, 23
Sulentic, J. W., Marziani, P., & Calvani, M. 2001, in AIP Conf. Proc. 599, X-ray Astronomy: Stellar Endpoints, AGN, and the Diffuse X-ray Background (Melville, NY: AIP), 963
Sulentic, J. W., Marziani, P., del Olmo, A., et al. 2014, AAp, in press (arXiv:1406.5920)
Sulentic, J. W., Marziani, P., & Dultzin-Hacyan, D. 2000, ARA&A, 38, 521
Sulentic, J. W., Marziani, P., Zamanov, R., et al. 2002, ApJL, 566, L71
Sulentic, J. W., Marziani, P., Zamfir, S., & Meadows, Z. A. 2012, ApJL, 752, L7
Sulentic, J. W., Repetto, P., Stirpe, G. M., et al. 2006b, A&A, 456, 929
Trevese, D., Paris, D., Stirpe, G. M., Vagnetti, F., & Zitelli, V. 2007, A&A, 470, 491
Tytler, D., & Fan, X.-M. 1992, ApJS, 79, 1
Vanden Berk, D. E., Richards, G. T., Bauer, A., et al. 2001, AJ, 122, 549
Véron-Cetty, M.-P., Véron, P., & Gonçalves, A. C. 2001, AAp, 372, 730
Vestergaard, M., & Peterson, B. M. 2006, ApJ, 641, 689
Vestergaard, M., & Wilkes, B. J. 2001, ApJS, 134, 1
Wandel, A., Peterson, B. M., & Malkan, M. A. 1999, ApJ, 526, 579
Wang, H., Wang, T., Zhou, H., et al. 2011, ApJ, 738, 85
Wills, B. J., Brotherton, M. S., Fang, D., Steidel, C. C., & Sargent, W. L. W. 1993, ApJ, 415, 563
Wills, D., & Netzer, H. 1979, ApJ, 233, 1
Woo, J.-H., Treu, T., Barth, A. J., et al. 2010, ApJ, 716, 269
Woosley, S. E., & Weaver, T. A. 1995, ApJS, 101, 181
Zamfir, S., Sulentic, J. W., Marziani, P., & Dultzin, D. 2010, MNRAS, 403, 1759
Zhang, K., Dong, X.-B., Wang, T.-G., & Gaskell, C. M. 2011, ApJ, 737, 71